Michigan State University
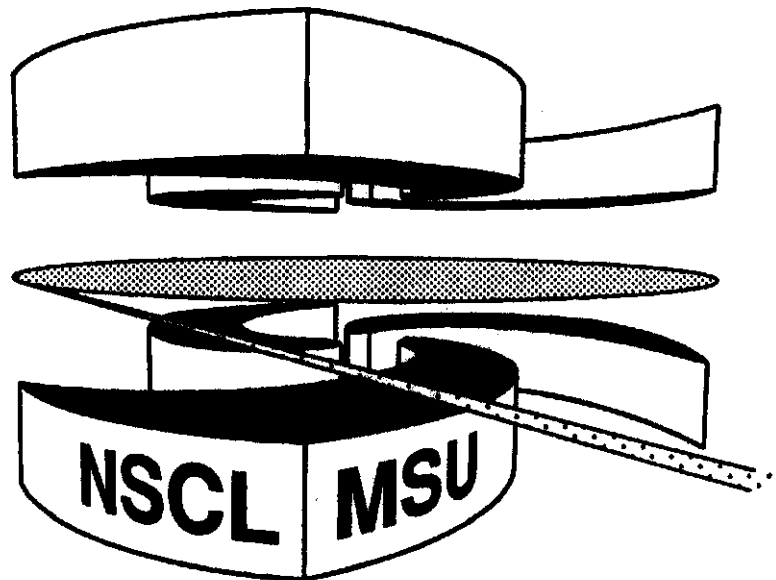
National Superconducting Cyclotron Laboratory

THE SPHERICITY OF CENTRAL HEAVY-ION REACTIONS

W.J. LLOPE

NSCL MSU

The sphericity of central heavy-ion reactions.

W.J. Llope[1,§], W. Bauer[1], D. Craig('), E. Gualtieri[1], S. Hannuschke[1], R.A. Lacey[2], J. Lauret[2], T. Li[1], C.M. Mader[7], A. Nadasen[3], E. Norbeck[6], R. Pak[1], G. Peilert[5], N. Stone[1], A.M. Vander Molen[1], G.D. Westfall[1], J. Yee[1], and S.J. Yennello[4].

(The NSCL 4π Group)

1. *National Superconducting Cyclotron Laboratory, Michigan State* University, *E. Lansing, MI* **48824**
2. *Deportment* **of** *Chemistry, State* **University** **Of** *New York • Stony Brook, Stony Brook, NY 11794*
3. *Department* **of** *Physics, U.* **of** *Michigan • Dearborn, Dearborn, MI* **48128**
4. *Cyclotron* **Institute,** *Texas A&M* University, College **Station,** *TX 77843*
5. *Lawrence Livermore National Laboratory, Livermore, CA 94550*
6. *Department* **of** *Physics and Astronomy, U.* of Iowa, *Iowa City, IA 52242*
7. *Department* **of** Physics, Hope College, *Holland, MI 49423*

December 21, 1994

PACS number(s): 25.70.-z.

ABSTRACT

We have experimentally studied small impact parameter heavy-ion collisions in the (nearly) symmetric entrance channels $^{12}C+^{12}C$, $^{20}Ne+^{27}Al$, $^{40}Ar+^{45}Sc$, $^{84}Kr+^{93}Nb$, and $^{129}Xe+^{139}La$, each at many intermediate beam energies. The results from a number of analyses based on a projection of the "shapes" of the experimental events called the sphericity are presented. Comparisons of the relative efficiencies of various experimental methods for the selection of central events are made. The importance of autocorrelations between the sphericity and the various impact-parameter variables is evaluated. Searches for possible beam energy-dependent transitions from sequential binary disassembly to multifragmentation in the central events are described. Comparisons to dynamic and hybrid model code calculations will be discussed. The average sphericities of the intermediate mass fragments (IMFs, for which $3 \leq Z \lesssim 20$), are presented. The possibility that the IMF emission occurs following the formation of transient toroidal or disk-like geometries in the central events in explored. Critical behavior, attributed to a transition from sequential binary disassembly to multifragmentation, is observed. The transitional beam energies for the central $^{40}Ar+^{45}Sc$, $^{84}Kr+^{93}Nb$, and $^{129}Xe+^{139}La$ reactions are near -50, -40, and -40 MeV/nucleon, respectively.

§Present Address: Bonner Nuclear Laboratory, Rice University, Houston, TX 77251-1892
E-mail Address: llope@physics.rice.edu

It is possible to form excited nuclear systems in the laboratory by colliding atomic nuclei. The impact parameter, as well as the predominant reaction mechanisms at each impact parameter, can be inferred from the experimentally measured characteristics of the particle emission. Given an efficient experimental selection of the most central collisions, beam energies from $\sim$10 to $\sim$150 MeV/nucleon can result in the formation of single nuclear systems with excitation energies from several to tens of MeV/nucleon. In such a range of excitation energies, previous experiments have indicated possible transitions between sequential binary (SB) disassembly mechanisms and multifragmentation (MF) (see Ref. [1] for recent reviews). Detailed theoretical calculations [2] [3] [4] have predicted that the equivalent of a proper liquid-gas phase transition in finite nuclear systems occurs at excitation energies on the order of 10 MeV/nucleon for systems of mass $\sim$100. The possibility that transitions in disassembly mode from SB to MF are an artifact of such a liquid-gas phase transition is, however, only one of many. Systematic experimental studies of the total mass and excitation energy dependence of the predominant disassembly mechanisms and the applicability of the various theoretical descriptions are therefore necessary. In this paper, such studies based on event shape analyses of a comprehensive set of experimental data are described.

The experimental data was collected using the MSU 4π Array [5] at the National Superconducting Cyclotron Laboratory. Reactions in the entrance channels ^{12}C+^{12}C, ^{20}Ne+^{27}Al, ^{40}Ar+^{45}Sc, ^{84}Kr+^{93}Nb, and ^{129}Xe+^{139}La were measured with a minimum bias trigger in 5-10 MeV/nucleon steps in beam energy, up to the maximum energy available from the K1200 Cyclotron for each projectile: 155, 140, 115, 75, and 60 MeV/nucleon, respectively. The lowest beam energies measured in each entrance channel were 55, 55, 15, 35, and 25 MeV/nucleon, respectively. Detailed descriptions of the data collection have already been published [6] [7].

The analyses of these data will proceed via the study of the average event shapes, which summarize aspects of the three-dimensional average patterns of the particle emission as viewed from the center of momentum (CM) frame. The cartesian components of the CM frame particle momenta, $p^{(k)}$, are used to fill a tensor, [8] $F_{ij} = \sum_k^N [p_i^{(k)} p_j^{(k)} / 2m_k]$, in each event. The normalization of the eigenvalues of this tensor, t_i, via $q_i = t_i^2 / \sum_{i=1}^3 t_i^2$, allows the calculation of the sphericity [9] using $S = \frac{3}{2}(1 - q_3)$, where q_3 is the largest normalized eigenvalue. All shape observables extracted from F_{ij}, e.g. S, depend strongly [10] on the number of particles, N, included in the sum in F_{ij}. For a given value of N, particle emission patterns that are isotropic in a momentum space coordinate system that spatially coincides with the CM frame have the largest possible sphericities, while otherwise deformed emission patterns have smaller sphericities.

Given methods to remove the dependence of S on N, it is possible to extract information concerning the impact parameter and the characteristics of the predominant reaction mechanisms from this observable. The sensitivity of the sphericity to the impact parameter is caused by the increasing probability for the emission of particles from spectator-like sources as the impact parameter is increased [11]. Particles emitted from such sources have relatively large momenta and forward/backward focussed emission angles when viewed from the CM frame, and hence strongly suppress the sphericity. Also, in the most central

collisions, SB disassembly of the excited system results in emission patterns that are more elongated in momentum space than those expected for MF reactions [9] [12]. In a region of excitation energy and mass for which the first decay step involves an (a)symmetric fission, the particles in the final state kinematically reflect the back-to-back trajectories of the two excited pre-fragments produced following the fission step.

The finite values of the multiplicities, N, and inefficiencies in the central event selection conspire to suppress $\langle S \rangle$, and to decrease the distinctions in average sphericity between SB and MF events. Concerning the former, we will therefore only present results following the placement of some constraint on the multiplicity of particles used in the calculation of the sphericity for each event. To limit the latter, we begin by investigating the relative efficiencies of various experimental methods for selecting the central collisions, which is described in Section 1. We present evidence for a beam energy dependent change in the predominant reaction mechanism in the central events in Section 1. Additional evidence for such a transition is described in Sections 2 and 3. Section 2 describes comparisons to the average sphericities of the filtered events from a number of SB and MF models, while Section 3 presents "subset sphericities". The possibility of the formation of transient toroidal or disk-shaped freeze-out configurations is also explored in Section 3. The summary and conclusions are presented in Section 4.

1 THE SELECTION OF CENTRAL COLLISIONS

The selection of the most central experimental collisions constrains the mass of the excited nuclear system and results in a monotonic relationship between the beam energy and the excitation energy in this system. Software cuts on global observables, i.e. centrality variables, that are assumed to be correlated with the impact parameter are used to select samples of the most central events. One must ensure, however, that the specific cut used to select these events is relatively inefficient at selecting larger impact parameter events with significant topological fluctuations, and does not autocorrelate with subsequent stages of the analysis.

In peripheral collisions, the kinetic energy and polar angle dependence of particle emission can be approximately parameterized as that from two independent thermal sources which move through the CM frame with projectile-like and target-like velocities. In such a picture, increasingly more central collisions result in larger cross sections for particle emission from a source at rest in the CM frame. The relative velocities of the spectator source frames and the CM frame lead to the appearance of large kinetic energies and strong forward-backward focussing of the particles emitted from spectator sources, when such emission is viewed from the CM frame. Particle emission from spectator-like sources thus elongates the shape of the event in the CM frame, and leads to severe suppressions of the sphericity that are related directly to the impact parameter.

The experimental selection of the most central collisions proceeds by the selection of those events with specific values of a global observable that is assumed to be monotonic with the impact parameter [13] [14]. Examples of such global observables ("centrality variables") are the measured total charged particle multiplicity N_{chgd}, the total charge

detected in a software gate centered at mid–rapidity, Z_{MR}, the proton multiplicity, N_p (which is complementary to the total charge bound in fragments, Z_{bound}), the total detected charge, Z_{det}, and the total transverse kinetic energy, KE_T. In the present study, all of these variables are defined as described in Refs. [13] and [14], with the exception of the variable complementary to Z_{bound}. The proton multiplicity, N_p, is used herein as the complement to the total charge in fragments with $A \geq 2$ (previously, the requirement $Z \geq 2$ was used, and the complement was the hydrogen multiplicity). For each of these observables, maximal values are assumed to occur in the smallest impact parameter collisions. From (approximate) geometrical arguments, the selection of the $\sim$10% [15] most central events results in average impact parameters of $\langle b \rangle \sim 0.3b_{max}$. The quantity b_{max} is the largest impact parameter satisfying, on average, the trigger condition that was used during the data collection, which was two charged particle hits for these data.

The average sphericities of the $\sim$10% [15] most central events selected by cuts on each of the different centrality variables is indicative of the relative strengths of the correlation between each centrality variable and the impact parameter. Two methods allowing the removal of the finite multiplicity distortions [10] to the average sphericities will be described.

The experimental semi-inclusive average sphericity, $\langle S_{inc} \rangle$, as a function of the total charged particle multiplicity is shown in Figure 1 for the reactions $^{12}C+^{12}C$, $^{20}Ne+^{27}Al$, $^{40}Ar+^{45}Sc$, $^{84}Kr+^{93}Nb$, and $^{129}Xe+^{139}La$. Each frame in this Figure contains the experimental dependence of the average semi-inclusive sphericity for many representative beam energies, including two extreme values, that were collected for each entrance channel. All of these curves exhibit sharp increases of the average sphericity for increasing multiplicities that result primarily from the finite multiplicity distortions.

A first method for investigating the relative efficiencies of the different centrality cuts starts with the measurement of these semi-inclusive average sphericities versus the charged particle multiplicity, $\langle S_{inc} \rangle(M)$, in a first pass through the data. Then, in a second pass, the charged particle multiplicity in each event, M, is used to locate the appropriate average semi-inclusive sphericity. A "reduced" sphericity is then defined for each event using $S_{red}(M) = S(M)/\langle S_{inc} \rangle(M)$, where S is the measured sphericity of the event. The values of these reduced sphericities averaged over the multiplicity, M, are, on the average, free from the finite multiplicity distortions by definition. Thus, the average reduced sphericities obtained by cuts on the different centrality variables imply the relative efficiencies by which these cuts minimize the impact parameters in the selected events.

The average reduced sphericity, $\langle S_{red} \rangle$, as a function of the "severity" of cuts on the different centrality variables for four representative beam energies in the $^{40}Ar+^{45}Sc$ entrance channel is depicted in Figure 2. The horizontal axis is defined as the probability that an event is selected versus a lower limit cut on each centrality variable separately, which corresponds to the fraction of the total trigger cross-section accepted by the cut. In each frame, the average sphericities at the far left thus correspond to the impact parameter inclusive values, and proceeding horizontally to the right implies increasingly larger thresholds, i.e. increasingly strict cuts on the largest values of each centrality variable. The centrality cuts which are compared are those placed on the variables N_{chgd} (solid lines),

Z_{MR} (short dashed), Z_{det} (dot dashed), N_p (dots dashed), and KE_T (dotted). We furthermore define as a centrality variable the total charge in hydrogen and helium fragments, Z_{LCP} (long dashed). Cuts placed on the centrality variable N_{chgd} (solid lines) result in average reduced sphericities equalling unity by definition.

For the 15 and 35 MeV/nucleon beam energies shown in Figure 2, the largest reduced sphericities are obtained for cuts in the centrality variables N_p and Z_{LCP}. Relative to cuts on the other centrality variables, cuts on these variables lead to the most spherical events. At larger beam energies in this entrance channel, cuts on the total transverse kinetic energy, KE_T, lead to the largest sphericities.

Cuts on the variable KE_T which are stricter than ~10% generally result in significantly lower average reduced sphericities than those when more moderate, i.e. ~10% [15], cuts are used. This behavior is independent of the entrance channel mass and the beam energy, and is attributed to a significant autocorrelation [7] between the transverse kinetic energy, KE_T, and the sphericity, S, which becomes important when events with extreme values of KE_T are selected via very strict cuts. Of all of the centrality variables studied here, strict KE_T cuts have the most direct effect on the flow tensor, and hence the sphericities that are obtained, as the tensor is calculated using the cartesian components of the kinetic energies of the particles in the event.

A significant autocorrelation [7] between a given centrality variable and the sphericity is also indicated by a relative suppression of the widths of the reduced sphericities, $\Delta S_{red} = \sqrt{[\langle S_{red}^2 \rangle - \langle S_{red} \rangle^2]}$, at specific multiplicities. These widths depend strongly on the multiplicity, but are independent of the centrality variable upon which the cut is made for each entrance channel and beam energy when ~10% [15] cuts are used. Autocorrelations between $\langle S_{red} \rangle$ and the various centrality variables are thus negligible for the present small impact parameter cuts. Stricter cuts (~1%) were seen to lead to larger differences between the widths of the sphericities of the events accepted by cuts on each of the different centrality variables (especially KE_T), and hence significant autocorrelations between $\langle S_{red} \rangle$ and the various centrality variables. Such autocorrelations bias significantly suppresses the average sphericities in the selected events.

An alternative method for extracting the relative efficiencies of the various centrality variables for the selection of the central events is now described. The average sphericities of the events passing the one dimensional ~10% [15] cuts described above is depicted in Figure 3 versus the charged particle multiplicity. The different line styles correspond to cuts on each of the different centrality variables that were shown in Figure 2, while the semi-inclusive average sphericities, i.e. Figure 1, are given by the crossed points. Four representative entrance channels and beam energies are shown: ^{20}Ne+^{27}Al at 55 MeV/nucleon, ^{40}Ar+^{45}Sc at 75 MeV/nucleon, ^{84}Kr+^{93}Nb at 55 MeV/nucleon, and ^{129}Xe+^{139}La at 55 MeV/nucleon. Significant differences between the average sphericities at specific multiplicities obtained from cuts on the different centrality variables are apparent.

To clarify these differences by removing the large variation resulting primarily from the finite multiplicity distortions, the ratios of the average sphericities in each sample of selected events (lines) and the semi-inclusive average sphericities (crossed points) are formed at each experimental multiplicity. Figures 4 through 8 depict these ratios for

four representative beam energies each in the ^{12}C+^{12}C, ^{20}Ne+^{27}Al, ^{40}Ar+^{45}Sc, ^{84}Kr+^{93}Nb, and ^{129}Xe+^{139}La entrance channels, respectively. By definition, the ratios of the average sphericities from an N_{chgd} cut and the semi-inclusive average sphericities is unity. The cuts on the other centrality variables generally allow events extending to lower multiplicities than those selected by cuts on N_{chgd}. The statistical error bars in these ratios are not plotted for every curve and each multiplicity for clarity. Only the statistical errors for the N_{chgd} cuts (solid) and the errors for the lowest multiplicity accepted by each of the other centrality cuts are drawn.

In the ^{12}C+^{12}C reactions at 55, 75, 115, and 155 MeV/nucleon (Figure 4), dramatically different average reduced sphericities are obtained from small impact parameter cuts on the different centrality variables. The average reduced sphericities from the KE_T cuts are generally the largest for all of the beam energies shown. Similar trends are visible in the ^{20}Ne+^{27}Al (Figure 5), and the ^{40}Ar+^{45}Sc (Figure 6) reactions for the same range of beam energies. However, at the lower beam energies in the ^{40}Ar+^{45}Sc entrance channel, the largest reduced sphericities are obtained from the cuts on the proton multiplicity, N_p. As the entrance channel mass increases, i.e. for the ^{84}Kr+^{93}Nb and ^{129}Xe+^{139}La reactions (Figures 7 and 8), the differences between the average reduced sphericities obtained from the different centrality cuts decreases, as compared to the lighter entrance channels at the same beam energies. The relative efficiencies of the different centrality variables therefore becomes similar as the entrance channel mass is increased.

To summarize the results of Figures 4 through 8 in a way that accounts for the different weighting of each of these curves by the different spectra of total charged particle multiplicities selected using each cut, the averages over each of these curves are formed using weights given by the number of counts in each bin of this selected multiplicity. As the finite multiplicity distortions have already been removed on the average from Figures 4 to 8, this weighted averaging over these curves is not affected by these distortions. The relative ordering of the weighted averages of the curves shown in Figures 4 to 8 is therefore indicative of the relative efficiencies of the various centrality variables for the selection of small impact parameter events.

These weighted averages are shown in Figure 9 as a function of the beam energy for all five entrance channels. All of the available beam energies were included in this Figure. In the two lightest entrance channels, ^{12}C+^{12}C and ^{20}Ne+^{27}Al, the largest weighted averages are obtained from cuts on KE_T and N_p for all of the available beam energies ($E_{proj} \geq 55$ MeV/nucleon). Transitions in the ordering of the relative efficiencies of the various centrality cuts are observed as a function of the beam energy in the ^{40}Ar+^{45}Sc, ^{84}Kr+^{93}Nb, and ^{129}Xe+^{139}La reactions. In each of these entrance channels, the smallest impact parameter events for beam energies below about 45 MeV/nucleon are most efficiently selected using cuts on the variables N_p and Z_{LCP}. Above this beam energy, the most efficient pairs of centrality variables are (KE_T, N_p), (KE_T, Z_{MR}), and (Z_{MR}, KE_T), for the ^{40}Ar+^{45}Sc, ^{84}Kr+^{93}Nb, and ^{129}Xe+^{139}La reactions, respectively.

The beam energy-dependent transitions in the most efficient means of selecting the central events seen in Figure 9 are assumed to be related to similarly beam energy-dependent transitions in the predominant reaction mechanisms at small impact parameters. Copious

light particle emission is expected from excited systems decaying by a sequential binary mechanism, due to the importance of the Coulomb and angular momentum barriers during such decays. Thus, one would expect that the most central collisions for an entrance channel and beam energy for which SB disassembly dominates would be those for which the largest light particle multiplicities were observed. A generally different reaction mechanism, i.e. one exhibiting distinct topological differences relative to SB events, might best be classified using centrality variables differing from those that best classify reactions leading to SB disassembly. The extent to which the transitions apparent in Figure 9 are indeed an artifact of transitions from SB to MF disassembly in the small impact parameter collisions is further investigated in the following Sections. Events were generated using SB and MF model codes and an accurate software replica of the apparatus, and direct comparisons to the experimental central events were made.

It is noted, however, that topological fluctuations in the events result in the allowance of some range of impact parameters for a specific value of an experimentally measured centrality variable. Events in which such fluctuations result in an underestimation of the impact parameter are a clear source of bias for one–dimensional centrality cuts. The use of two–dimensional centrality cuts would limit the contributions of such events [14]. Such a cut will henceforth be applied. These cuts select events in which the two most efficient centrality variables (from Fig. 9) exceed the $\sim$10% [15] thresholds used above. Generally, $\sim$4–8% of the minimum bias events ($\langle b \rangle / [R_P + R_T] \sim 0.2$–0.28 geometrically) are accepted.

2 COMPARISONS TO MODEL EVENTS

In this Section, events generated by a number of different model codes which embody either SB or MF disassembly are filtered through a detailed software replica of the MSU 4π Array and compared directly to the data. The event generation was performed in both dynamic (FREESCO [9]) and hybrid approaches, for which BUU [16] and QMD [17] calculations were used to describe the initial stages of the reactions. The "after-burners" used in the hybrid event generation were the Berlin [18] and Copenhagen [2] [19] MF codes, as well as the SB codes GEMINI [20] and SEQUENTIAL [21].

All of these codes were run with the default parameters with the exception of the charge, mass, and excitation energy in the composite system, which was extracted from the BUU calculations in the same manner as described in Ref. [22]. A soft equation of state was assumed, and the calculations were terminated when the radial density profile of the composite system most closely resembled that of a ground state nucleus [16]. The Berlin and GEMINI codes also require a cut-off angular momentum, which was taken as the maximum angular momentum that can be supported by the predicted composite system formed for each entrance channel and beam energy. These are in the range from $\sim$45$\hbar$ to $\sim$80$\hbar$, depending on the reaction.

The particle emission patterns from the MF models follow the assumption of an initially expanded and spherical freeze-out volume, and depend on the available phase space and the strong inter-particle Coulomb repulsion. Those from the SB models are relatively more elongated [9] [12], due to the assumed series of momentum conserving two-body

decay steps. Given means to remove the finite multiplicity distortions [10], the average sphericity of MF events exceeds that for events proceeding via SB disassembly [12].

For a given excited nucleus and at a specific final state multiplicity, the values of $\langle S \rangle$ for the events generated using the SEQUENTIAL(Berlin) code should agree with those from the GEMINI(Copenhagen) codes, and this was found to be true to about the ~10% level. Thus, for clarity in the Figures below, only the results using the MF code Berlin [18] and SB code SEQUENTIAL [21] will be plotted. The average sphericities from the dynamic MF model FREESCO, and the hybrid MF models QMD+Copenhagen, and BUU+Copenhagen also agree to within ~10% at specific multiplicities, implying a relative insensitivity of the present shape comparisons to the model chosen for the description of the initial stages of the reactions.

As opposed to the analyses in the previous Section, the finite multiplicity distortions to the average sphericities are removed from all of the following results graphically. The sphericities from the data and the model calculations will be plotted as a function of the number of particles included in the calculation of this observable. Comparisons between the experimental and model results are thus performed at specific values of this multiplicity, and are hence free from the finite multiplicity distortions [10].

By assumption, the average sphericities of the selected experimental events cannot be below the predictions of the SB model calculations, or above the predictions of the MF models. An increase in the average sphericity, relative to the predictions of the SB models, towards the predictions of the MF models with increases in the beam energy is indicative of an evolution of the reaction mechanism from SB disassembly to MF.

The average sphericities of the central experimental(generated) events are plotted versus the measured(filtered) total charged particle multiplicity in Figures 10, 11, and 12 for the ^{40}Ar+^{45}Sc, ^{84}Kr+^{93}Nb, and and ^{129}Xe+^{139}La reactions, respectively. The crossed points depict the results for the central experimental events, while the solid(dashed) lines are the results from the filtered MF(SB) model events.

The average sphericities of the central ^{40}Ar+^{45}Sc reactions at beam energies near and below 45 MeV/nucleon are in agreement with those predicted by the SB codes. The data jump from the SB to the MF predictions for multiplicities on the order of eight between the beam energies of 45 and 65 MeV/nucleon. At larger multiplicities in this entrance channel, a dramatic suppression to below the SB model predictions is visible. This implies a failure in one or more of the assumptions used in the present event generation for these high multiplicity events in this entrance channel. This suppression is further investigated in the next Section.

In the central ^{84}Kr+^{93}Nb and ^{129}Xe+^{139}La reactions, the average sphericities from the data are always between the predictions of the filtered SB and MF models for all available beam energies. For the central ^{129}Xe+^{139}La reactions (Figure 12), the average sphericities increase, relative to the SB predictions, with the increases in the beam energy. For beam energies near and above ~40 MeV/nucleon, the experimental average sphericities are in remarkable agreement with the MF model predictions over the entire range of multiplicities. Similar increases in the average sphericities of the central ^{84}Kr+^{93}Nb events (Figure 11) are also observed, although the model calculations tend to overpredict the total charged

particle multiplicities for these reactions.

3 SUBSET SHAPES

In this Section, the sphericity of particular subsets of an event will be distinguished from the sphericity of all of the particles in the event. This will allow more stringent tests of the accuracy by which the present model calculations reproduce the average sphericities of the experimental events. It is important to note that the sphericities of such event subsets are affected to some degree by the fact that the total momentum of a particular subset need not be conserved. Another source of bias to the subset sphericities would clearly contribute if the subset was defined on the basis of some kinematical aspect of the event. The simulations described in the previous Section indicate, however, that reasonably general definitions of subsets based on the particle charges do not suffer from significant bias from either of these effects. Examples of two such subsets are the LCPs and IMFs. Light particle emission is probable throughout the reaction, including that from the pre-equilibrium stages as well as in secondary decays of excited fragments far from the collision zone and long after freeze-out. The emission of IMFs, on the other hand, is more a reflection of the excited composite system and its expansion to low densities, so we concentrate on the average sphericities of the IMFs in this Section.

The previous Section noted that the average sphericities of the largest multiplicity central events in the ^{40}Ar+^{45}Sc (and lighter) reactions were significantly below the predictions of the present SB model calculations. For all of the available entrance channels and beam energies, the largest average multiplicities of IMFs are found in the events with the largest total charged particle multiplicities [7]. As depicted in Figure 13, the average IMF sphericities, $\langle S_{IMF} \rangle$, are generally well below the those predicted by the filtered SB model calculations for all IMF multiplicities. As the emission of IMFs is the most important at the largest charged particle multiplicities, these suppressed IMF sphericities effect the suppression at large charged particle multiplicities seen in Fig. 10. A similar suppression of the IMF sphericities to below the SB model predictions was also observed for the central ^{12}C+^{12}C and ^{20}Ne+^{27}Al reactions. We will return to a discussion of this suppression of the IMF sphericities for these (light) entrance channels near the end of this Section.

The IMF sphericities in the central ^{84}Kr+^{93}Nb reactions are in good agreement with the SB model predictions for the 35 MeV/nucleon data. They increase, relative to the SB model predictions, with increases in the beam energy, coming to quantitative agreement with the MF model predictions for beam energies near and above 65 MeV/nucleon. For the central ^{129}Xe+^{139}La reactions, the average IMF sphericities are always between the SB and MF model predictions. Good agreement between the experimental IMF sphericities and the MF model predictions are observed for beam energies above $\sim$40 MeV/nucleon.

The beam energy dependence of the average IMF sphericities are shown in Figure 16 for specific IMF multiplicities in the central ^{40}Ar+^{45}Sc, ^{84}Kr+^{93}Nb, and ^{129}Xe+^{139}La reactions. Some points in the upper frame of Figure 16 have been vertically offset by the amounts shown for clarity, while the solid lines in all three frames are included only to guide the eye. In the central ^{40}Ar+^{45}Sc reactions, a significant increase in the average IMF sphericities

is observed at beam energies near 55 MeV/nucleon for all IMF multiplicities. A similar increase of the IMF sphericities is also observed in the central ^{129}Xe+^{139}La reactions at beam energies near 40 MeV/nucleon. In the ^{84}Kr+^{93}Nb entrance channel, the average IMF sphericity for each value of N_{IMF} increases when going from 35 to 45 MeV/nucleon in beam energy, and is constant for beam energies from 45 to 75 MeV/nucleon. Similar, although less pronounced, maxima in the average sphericities of all of the particles in the selected events were also observed at the same beam energies that lead to maximal IMF sphericities.

As noted above, the IMF emission patterns in the ^{12}C+^{12}C, ^{20}Ne+^{27}Al, and ^{40}Ar+^{45}Sc entrance channels are far more deformed than that expected from the SB (or MF) model calculations. It is possible to imagine several possible causes for this effect. The first concerns impact parameter fluctuations. In the lightest entrance channels, there is simply not much information available upon which to base a centrality cut. An (integer) centrality variable's bin-width may be a significant fraction of the maximum value in the spectrum populated in the minimum bias events. As noted in Ref. [14], this leads to relatively larger fluctuations in the impact parameters deduced for each event. If this were the only possibility, a breakdown in the geometrical assumption that the maximal 4–8% of the minimum bias events corresponds to $\langle b \rangle / [R_P + R_T] \sim$ 0.2–0.28 in the light entrance channels would be evident. The second possibility assumes that fluctuations in the initial stages of the reactions increase in importance as the entrance channel mass is decreased. In those collisions for which the equilibration of the excited composite system is particularly incomplete, some knowledge of the initial trajectories of the projectile and target nuclei could be retained by the particles in the final state. Prolate shapes oriented along the beam direction would be expected for such events, in similarity to that expected given significant contaminations to the samples of selected central events from more peripheral collisions.

The third possibility assumes the formation of non-compact geometries other than bubbles, e.g. toroids, [23] at freeze-out. In the context of shape analyses, these freeze-out configurations should result in coplanar IMF emission patterns with the IMF flow angles $\theta_2 = \cos^{-1}(t_2 \cdot \hat{z})$ and $\theta_3 = \cos^{-1}(t_3 \cdot \hat{z})$ near 90°, where $\hat{z}$ is the incident beam axis and $t_2(t_3)$ is the IMF eigenvector corresponding to the second largest(largest) eigenvalue. The average IMF coplanarity, $C_{IMF} = \frac{\sqrt{3}}{2}(q_2 - q_1)$, and flatness, $F_{IMF} = \frac{\sqrt{3}}{2}(t_2 - t_1)/(\sum_{i=1}^{3} t_i)$, should exceed that from an isotropic IMF emitter. One would furthermore expect that C_{IMF} and F_{IMF} would increase both with the IMF flow angle, θ_3, and the sum $\theta_3 + \theta_2$ (for specific values of N_{IMF}).

Other aspects of the average shapes of the IMFs in the central events were studied to investigate these three possibilities. The IMF shapes in the selected ^{40}Ar+^{45}Sc events (and in the lighter entrance channels) are manifestly prolate. For all values of N_{IMF}, the central event averaged probability that $t_3 - t_2 > t_2 - t_1$, corresponding to prolate IMF emission patterns, increases significantly for decreasing entrance channel mass. These probabilities are shown in Figure 17. The CM frame ratios $\langle KE \rangle / 1.5 \langle KE_T \rangle$ are shown versus the particle charge in Figure 18. A prolate(oblate) pattern with the symmetry axis near the beam axis will result in $\langle KE \rangle / 1.5 \langle KE_T \rangle > (<) 1$, while a spherical pattern will result in

values near unity. The experimental values of this ratio in the selected events increase with decreasing entrance channel mass.

These observations point to an increase in the probability that the IMF emission patterns are elongated along the beam direction as the entrance channel mass is decreased, despite the restrictive central event selection described in Section 1. This is taken to imply an increase in the importance of impact parameter fluctuations, and/or an increase in the fluctuations in the initial stages of the reactions, as the entrance channel mass is decreased. This observation makes remote the possibility that the IMF emission in these data proceeds via a non-compact geometry that is oblate and expanding in the X-Y plane, as suggested by various transport calculations [23] [24] [25].

Further evidence that the observed IMFs do not freeze-out from a toroidal (or disk) shaped system is provided by Figures 14 and 15. Such geometries have been seen in various BUU calculations [23] [24] [25] of central collisions in entrance channels that are the same or similar to the ^{84}Kr+^{93}Nb and ^{129}Xe+^{139}La reactions studied here. However, the IMF sphericities observed in these entrance channels are consistent with the predictions of the present MF model calculations, which assume an expanded, but spherical, freeze-out volume.

It has been noted [25] that an observed absence of such planar configurations and the observation of spherical IMF emission is a statement that the nuclear equation of state is "soft" ($K_\infty \sim 215$ MeV). We note however that, if the IMFs that freeze-out of such a torus or disk expand (in the X-Y plane) with a transverse energy less than a few MeV/nucleon for beam energies above ~ 50 MeV/nucleon, then they would be more forward of the acceptance of the 4π Array in its present configuration.

4 SUMMARY AND CONCLUSIONS

This work concentrated on a particular projection, called the sphericity, of the shapes in momentum space of events from central heavy-ion reactions. A data set that is comprehensive both in the entrance channel mass and the beam energy was studied.

The relative efficiencies of many different methods for the selection of the small impact parameter events was investigated first. The particular choice of the global observable upon which centrality cuts are placed was shown to significantly affect the sphericities of the events that are selected. The most efficient centrality variables were assumed to result in the most spherical events, following the removal of the finite multiplicity distortions [10] to the average sphericities. Two new methods were described that allow the removal, on the average, of these distortions. This allowed a ranking of the relative efficiencies of the different centrality variables for the selection of small impact parameters to be experimentally accessible. Transitions in the variables that best select the most central events were observed in the three heaviest entrance channels, which is indicative of significant changes in the topology of the central events. This was presumed to be indicative of changes in the predominant reaction mechanism, and was further investigated in the remainder of this paper. Autocorrelations [7] between the average sphericity and the various centrality variables were also investigated, and were shown to be negligible for the $\sim 10\%$ [15] cuts

used in the present analyses.

The average sphericities of the entire events, and of a particular subset of the events (the IMFs), were compared to those predicted by a variety of SB and MF model codes. Unlike the studies of *relative* sphericities described in Section 1, these comparisons allowed tests of the absolute scale of average sphericities from the data and the models. Transitions from SB disassembly to MF were observed on the basis of these comparisons. However, the IMF emission in the light entrance channels is prolate along the beam direction, despite the restrictive selection of central events that was performed. In the heavier entrance channels and for beam energies above ~40 MeV/nucleon, the IMF emission is consistent with the predictions of the MF models, which assume an expanded and spherical freeze-out configuration. This casts doubt on the transport model predictions of freeze-out configurations that are tori or disks and expanding in the X-Y plane.

There are no indications of such transitional behavior in the available central ^{12}C+^{12}C and ^{20}Ne+^{27}Al reactions ($E_{proj} \geq 55$ MeV/nucleon). The qualitatively located beam energies at which the various analyses described in this paper indicated critical phenomena in the central ^{40}Ar+^{45}Sc, ^{84}Kr+^{93}Nb, and ^{129}Xe+^{139}La reactions are depicted in Figure 19. Also included in this Figure is the critical beam energy observed by Cebra *et al.* for central ^{40}Ar+^{51}V reactions [21], and the critical beam energies observed in a charge correlations analysis of the present data [26]. In this analysis, a clear transition in the relative sizes of the three largest fragments in central events is observed at beam energies of 47±10, 35±10, and 32±5 MeV/nucleon in the ^{40}Ar+^{45}Sc, ^{84}Kr+^{93}Nb, and ^{129}Xe+^{139}La entrance channels, respectively.

The various analyses indicate similar transitional beam energies for each entrance channel. The transitional beam energies observed for the central ^{40}Ar+^{45}Sc reactions are significantly larger than those observed for the central ^{84}Kr+^{93}Nb and ^{129}Xe+^{139}La reactions.

The most obvious possibilities for this trend concern the open questions raised in Section 2 and 3. These involve an increasing importance of fluctuations in impact parameter, or in the degree of equilibration of the excited systems formed at one impact parameter, for decreasing entrance channel mass. Two other possibilities are noted, which should not, however, be considered until the two above have been fully explored. The third assumes an increase in the importance of quantum mechanical finite-size effects for the excited systems formed in increasingly lighter entrance channels. The fourth involves the fact that increasingly heavier entrance channels result in excited systems that are increasingly more proton-rich. The model calculations described in Section 2 predict a significant decrease in the transitional beam energy with an increase in the Coulomb energy of a nuclear system of fixed total mass. Experiments in several entrance channels of constant total mass but differing charge/mass ratios would be needed to verify this prediction.

5 ACKNOWLEDGEMENTS

References

[1] H. Fuchs and K. Möhring, Rep. Prog. Phys. **57**, 231 (1994), and references therein;

L.G. Moretto and G.J. Wozniak, Ann. Rev. Nucl. Part. Sci. (May, 1993), and references therein;

D.H.E. Gross, Rep. Prog. Phys. **53**, 605 (1990), and references therein;

E. Saraud, Ch. Grégoire, and B. Tamain, Prog. Nucl. Part. Sci. **23**, 357 (1989), and references therein.

[2] J.P. Bondorf, R. Donangelo, I.N. Mushustin, C.J. Pethick, H. Schulz, and K. Sneppen, Nucl. Phys. **A443**, 321 (1985);

J.P. Bondorf, R. Donangelo, I.N. Mushustin, and H. Schulz, Nucl. Phys. **A444**, 460 (1985);

H.W. Barz, J.P. Bondorf, R. Donangelo, I.N. Mushustin, and H. Schulz, Nucl. Phys. **A448**, 753 (1986).

[3] A.S. Botvina, I.S. Iljinov, I.N. Mushustin, J.P. Bondorf, R. Donangelo, and K. Sneppen, Nucl. Phys. **A475**, 663 (1987).

[4] W. Bauer, Phys. Rev. C **38**, 1297 (1988).

[5] G.D. Westfall, J.E. Yurkon, J. Van Der Plicht, Z.M. Koenig, B.V. Jacak, R. Fox, G.M. Crawley, M.R. Maier, B.E. Hasselquist, R.S. Tickle, and D. Horn, Nucl. Inst. and Methods **A238**, 347 (1985).

M. Maier, M. Robertson, A. Vander Molen, and G.D. Westfall, Nucl. Inst. and Methods **A337**, 619 (1994).

A.M. Vander Molen, R. Au, R. Fox, and S. Hannuschke, IEEE Trans. Nucl. Sci. **41**, 80 (1994).

[6] G.D. Westfall, W. Bauer, D. Craig, M. Cronqvist, E. Gualtieri, S. Hannuschke, D. Klakow, T. Li, T. Reposeur, A.M. Vander Molen, W.K. Wilson, J.S. Winfield, J. Yee, S.J. Yennello, R.A. Lacey, A. Elmaani, J. Lauret, A. Nadasen, and E. Norbeck, Phys. Rev. Lett. **71**, 1986 (1993);

E. Bauge, A. Elmaani, R.A. Lacey, J. Lauret, N.N. Ajitanand, D. Craig, M. Cronqvist, E. Gualtieri, S. Hannuschke, T. Li, W.J. Llope, T. Reposeur, A.M. Vander Molen, G.D. Westfall, J.S. Winfield, J. Yee, S.J. Yennello, A. Nadasen, and E. Norbeck, Phys. Rev. Lett. **70**, 3705 (1993);

T. Li, W. Bauer, D. Craig, M. Cronqvist, E. Gualtieri, S. Hannuschke, R.A. Lacey, W.J. Llope, T. Reposeur, A.M. Vander Molen, G.D. Westfall, W.K. Wilson, J.S. Winfield, J. Yee, S.J. Yennello, A. Nadasen, R.S. Tickle, E. Norbeck, Phys. Rev. Lett. **70**, 1924 (1993);

R.A. Lacey, A. Elmaani, J. Lauret, T. Li, W. Bauer, D. Craig, M. Cronqvist, E. Gualtieri, S. Hannuschke, T. Reposeur, A.M. Vander Molen, G.D. Westfall, W.K. Wilson, J.S. Winfield, J. Yee, S.J. Yennello, A. Nadasen, R.S. Tickle, and E. Norbeck, Phys. Rev. Lett. **70**, 1224 (1993).

[7] W.J. Llope, J.A. Conrad, C.M. Mader, G. Peilert, W. Bauer, D. Craig, E. Gualtieri, S. Hannuschke, R.A. Lacey, J. Lauret, T. Li, A. Nadasen, E. Norbeck, R. Pak, N. Stone, A.M. Vander Molen, G.D. Westfall, J. Yee, and S.J. Yennello, Physical Review C (in press), MSU Preprint MSUCL-908.

[8] M. Gyulassy, K.A. Frankel, and H. Stöcker, Phys. Lett. **110B**, 185 (1982).

[9] G. Fái and J. Randrup, Nucl. Phys. **A381**, 557 (1982);

G. Fái and J. Randrup, Nucl. Phys. **A404**, 551 (1983).

[10] P. Danielewicz and M. Gyulassy, Phys. Lett. **129B**, 283 (1983);

J.P. Bondorf, C.H. Dasso, R. Donangelo, and G. Pollarolo, Phys. Lett. B **240**, 28 (1990).

[11] H. Stöcker, G. Buchwald, L.P. Csernai, G. Graebner, J.A. Maruhn, and W. Greiner, Nucl. Phys. **A387**, 205c (1982).

[12] J. A. López and J. Randrup, Nucl. Phys. **A491**, 477 (1989).

[13] C.A. Ogilvie, D.A. Cebra, J. Clayton, S. Howden, J. Karn, A. Vander Molen, G.D. Westfall, W.K. Wilson, and J.S. Winfield, Phys. Rev. C **40**, 654 (1989).

[14] L. Phair, D.R. Bowman, C.K. Gelbke, W.G. Gong, Y.D. Kim, M.A. Lisa, W.G. Lynch, G.F. Peaslee, R.T. de Souza, M.B. Tsang, and F. Zhu, Nucl. Phys. **A548**, 489 (1992).

[15] It is not always possible to select a specific fraction of the impact parameter inclusive events, as often the case for centrality variables that are integer quantities. The threshold on a centrality variable chosen was the lowest possible bin for which <10% of the minimum bias events are in and above this bin. Generally, 7–10% of the events are selected by these cuts.

[16] C.M. Mader, Ph.D. Thesis, Michigan State University, unpublished (1993);

W. Bauer, G.F. Bertsch, W. Cassing, and U. Mosel, Phys. Rev. C **34**, 2127 (1986);

W. Bauer, Phys. Rev. Lett. **61**, 2534 (1988).

[17] J. Aichelin and H. Stöcker, Phys. Lett. B **176**, 14 (1986);

J. Aichelin, G. Peilert, A. Bohnet, A. Rosenhauer, H. Stöcker, and W. Greiner, Phys. Rev. C **37**, 2451 (1988);

G. Peilert, J. Konopka, H. Stöcker, W. Greiner, M. Blann, and M.G. Mustafa, Phys. Rev. C **46**, 1457 (1992).

[18] A.R. DeAngelis and D.H.E. Gross, private communication;

D.H.E. Gross, Prog. Part. Nucl. Phys. **30**, 155 (1993), and references therein;

X.-Z. Zhang, D.H.E. Gross, S.-Y. Xu, and Y.-M. Zheng, Nucl. Phys. **A461**, 641 (1987);

X.-Z. Zhang, D.H.E. Gross, S.-Y. Xu, and Y.-M. Zheng, *ibid.*, 668 (1987).

[19] H.W. Barz, D.A. Cebra, H. Schulz, and G.D. Westfall, Phys. Lett. B **267**, 317 (1991).

[20] R.J. Charity, M.A. McMahan, G.J. Wozniak, R.J. McDonald, L.G. Moretto, D.G. Sarantites, L.G. Sobotka, G. Guarino, A. Pantaleo, L. Fiore, A. Gobbi, and K.D. Hildenbrand, Nucl. Phys. **A483**, 371 (1988).

[21] D.A. Cebra, S. Howden, J. Karn, A. Nadasen, C.A. Ogilvie, A. Vander Molen, G.D. Westfall, W.K. Wilson, and J.S. Winfield, Phys. Rev. Lett. **64**, 2246 (1990).

[22] D.R. Bowman, C.M. Mader, G.F. Peaslee, W. Bauer, N. Carlin, R.T. de Souza, C.K. Gelbke, W.G. Gong, Y.D. Kim, M.A. Lisa, W.G. Lynch, L. Phair, M.B. Tsang, C. Williams, N. Colonna, K. Hanold, M.A. McMahan, G.J. Wozniak, L.G. Moretto, and W.A. Friedman, Phys. Rev. C **46**, 1834 (1992).

[23] W. Bauer, G.F. Bertsch, and H. Schulz, Phys. Rev. Lett. **69**, 1888 (1992);

L.G. Moretto, K. Tsuo, N. Colonna, and G.J. Wozniak, *ibid*, 1884 (1992).

[24] L. Phair, W. Bauer, and C.K. Gelbke, Phys. Lett. B **314**, 271 (1994);

T. Glasmacher, C.K. Gelbke, and S. Pratt, Phys. Lett. B **314**, 265 (1993);

D.H.E. Gross, B.-A. Li, and A.R. DeAngelis, Annalen der Physik, **1**, 467 (1992);

S.R. Souza and C. Ngô, Phys. Rev. C (submitted).

[25] H.M. Xu, J.B. Natowitz, C.A. Gagliardi, R.E. Tribble, C.Y. Wong, and W.G. Lynch, Phys. Rev. C **48**, 933 (1993).

[26] N. Stone, W.J. Llope, and G.D. Westfall, Physical Review C (submitted), MSU Preprint MSUCL-916.
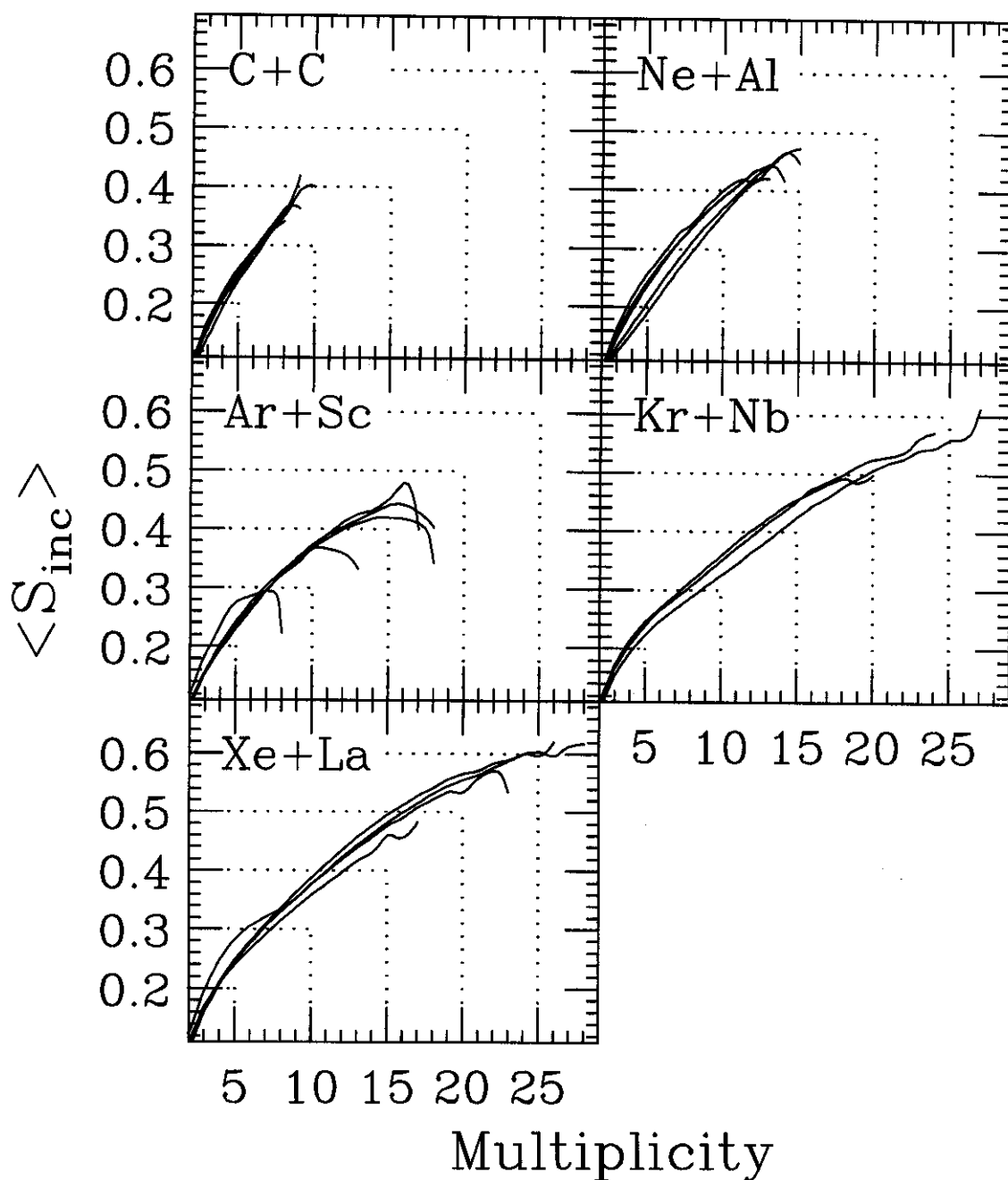
Figure 1: The experimental semi-inclusive average sphericity as a function of the charged particle multiplicity for the reactions $^{12}C+^{12}C$ at 55, 75, 115, and 155 MeV/nucleon, $^{20}Ne+^{27}Al$ at 55, 75, 95, 115 and 135 MeV/nucleon, $^{40}Ar+^{45}Sc$ at 15, 35, 75, 95, and 115 MeV/nucleon, $^{84}Kr+^{93}Nb$ at 35, 45, 55, and 75 MeV/nucleon, and $^{129}Xe+^{139}La$ at 25, 35, 45, and 55 MeV/nucleon.

Ar + Sc
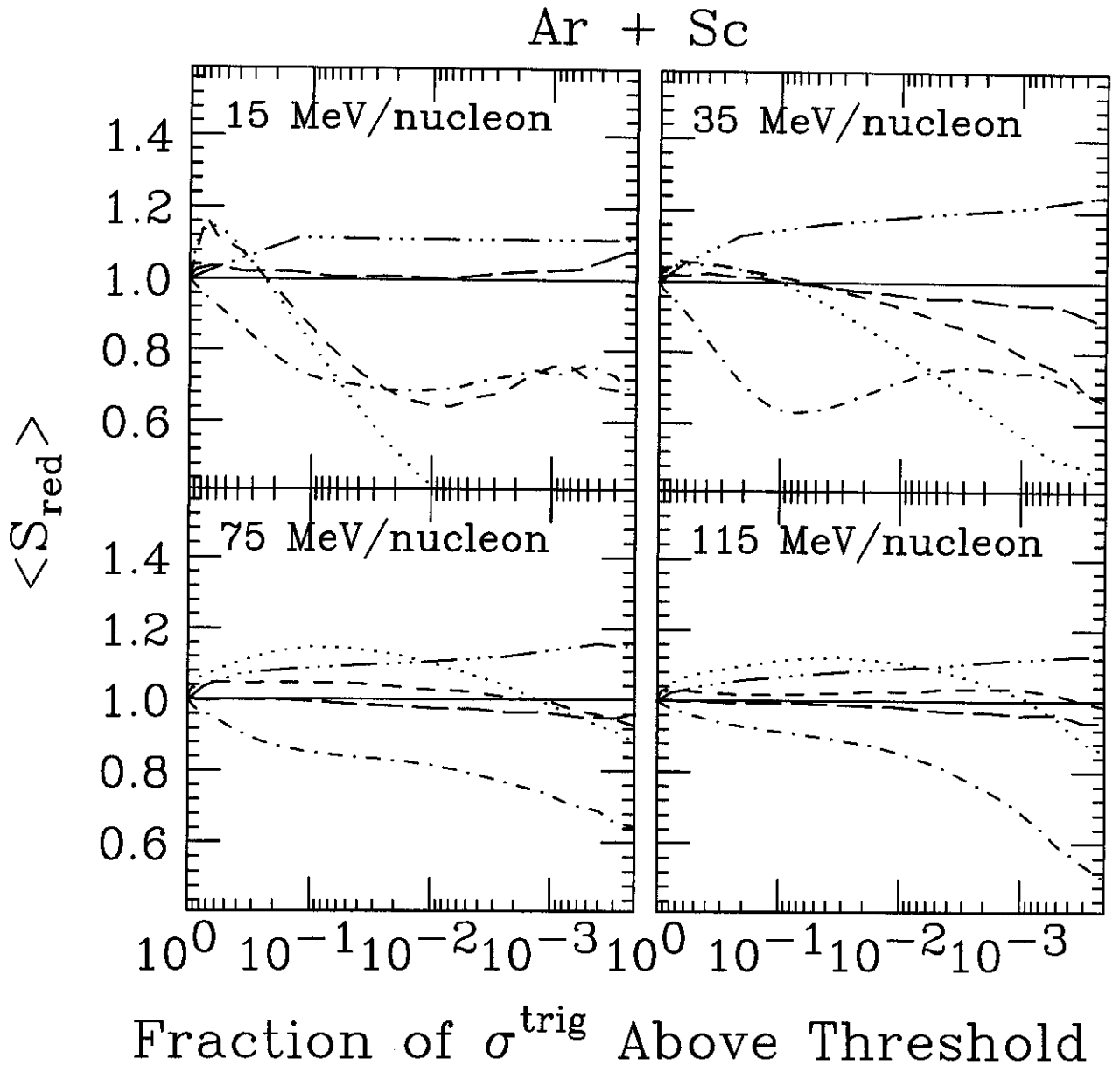
Figure 2: The average reduced sphericity as a function of the "severity" (see text) of centrality cuts placed on N_{chgd} (solid), Z_{LCP} (long dashed), Z_{MR} (short dashed), Z_{det} (dot dashed), N_p (dots dashed), and KE_T (dotted), for the $^{40}Ar+^{45}Sc$ reactions at 15, 35, 75, and 115 MeV/nucleon.
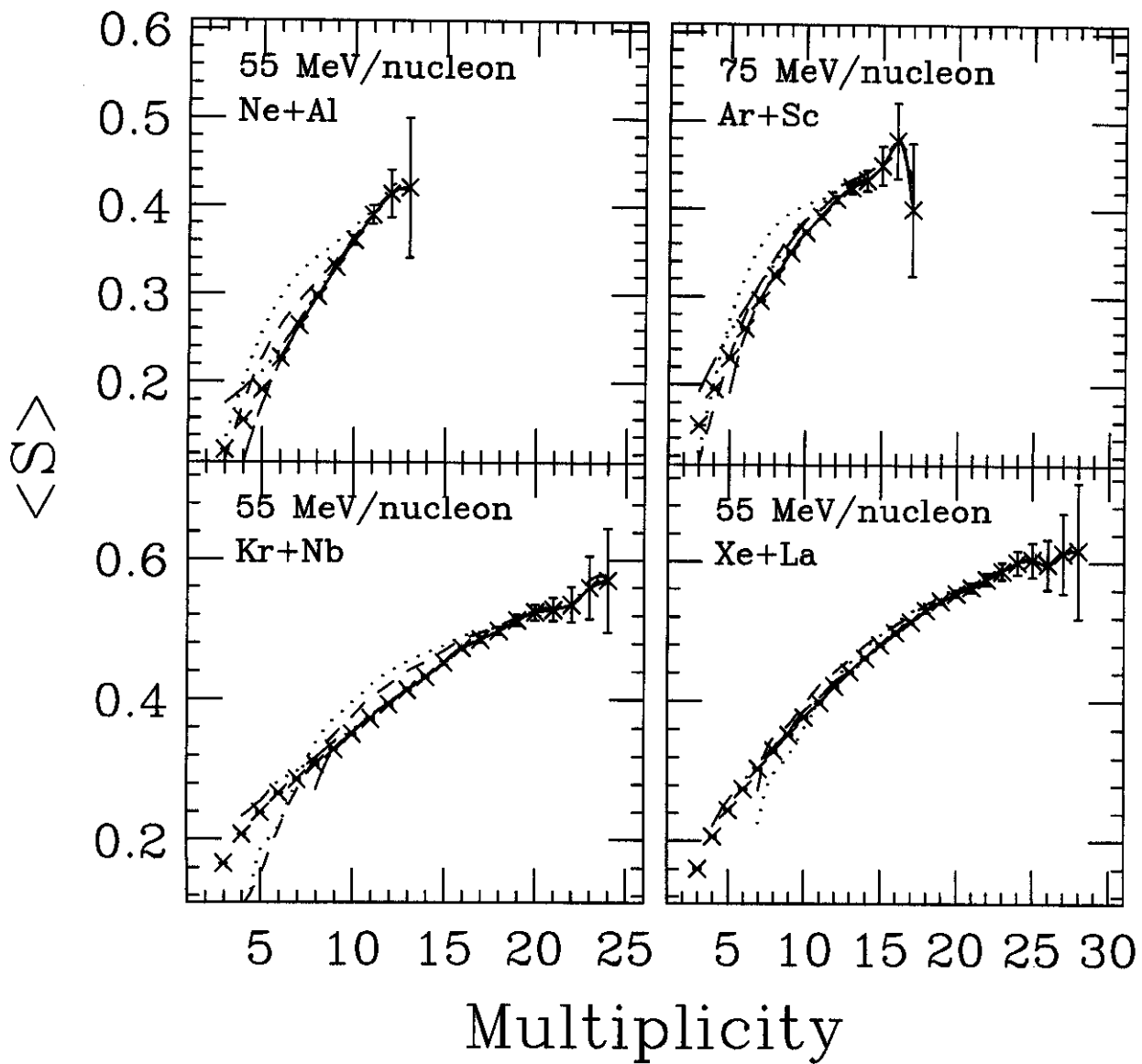
Figure 3: The semi-inclusive average sphericities versus the multiplicity (crossed points), and the average sphericities for those events selected by one–dimensional cuts on each of the various centrality variables which accept 10% of the events (lines). The line styles are as defined above.

C + C
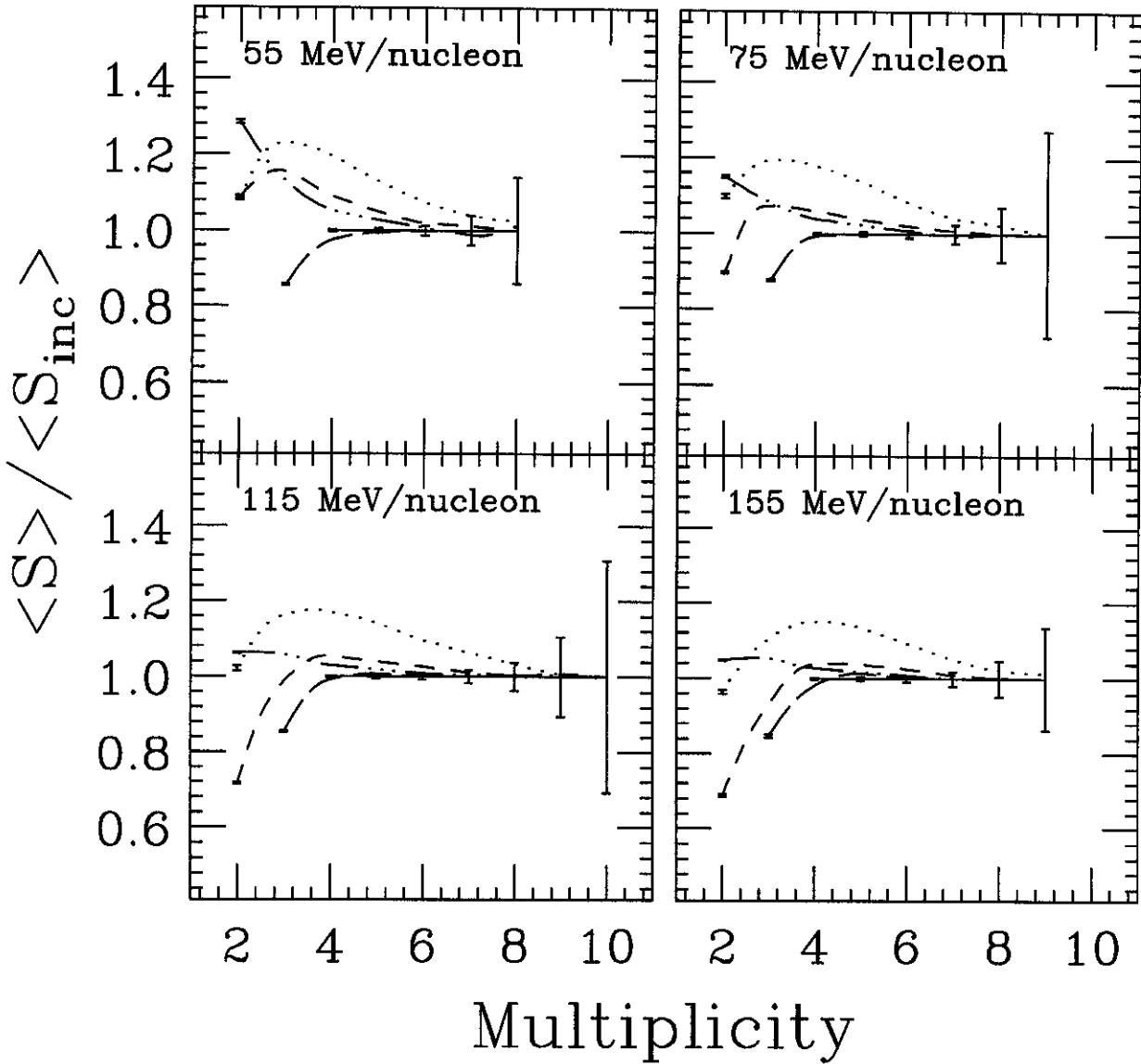
Figure 4: The ratios of the average sphericities selected by ~10% cuts on each of the various centrality variables to the semi-inclusive average sphericities as a function of the multiplicity for the $^{12}C+^{12}C$ reactions at beam energies of 55, 75, 115, and 155 MeV/nucleon.
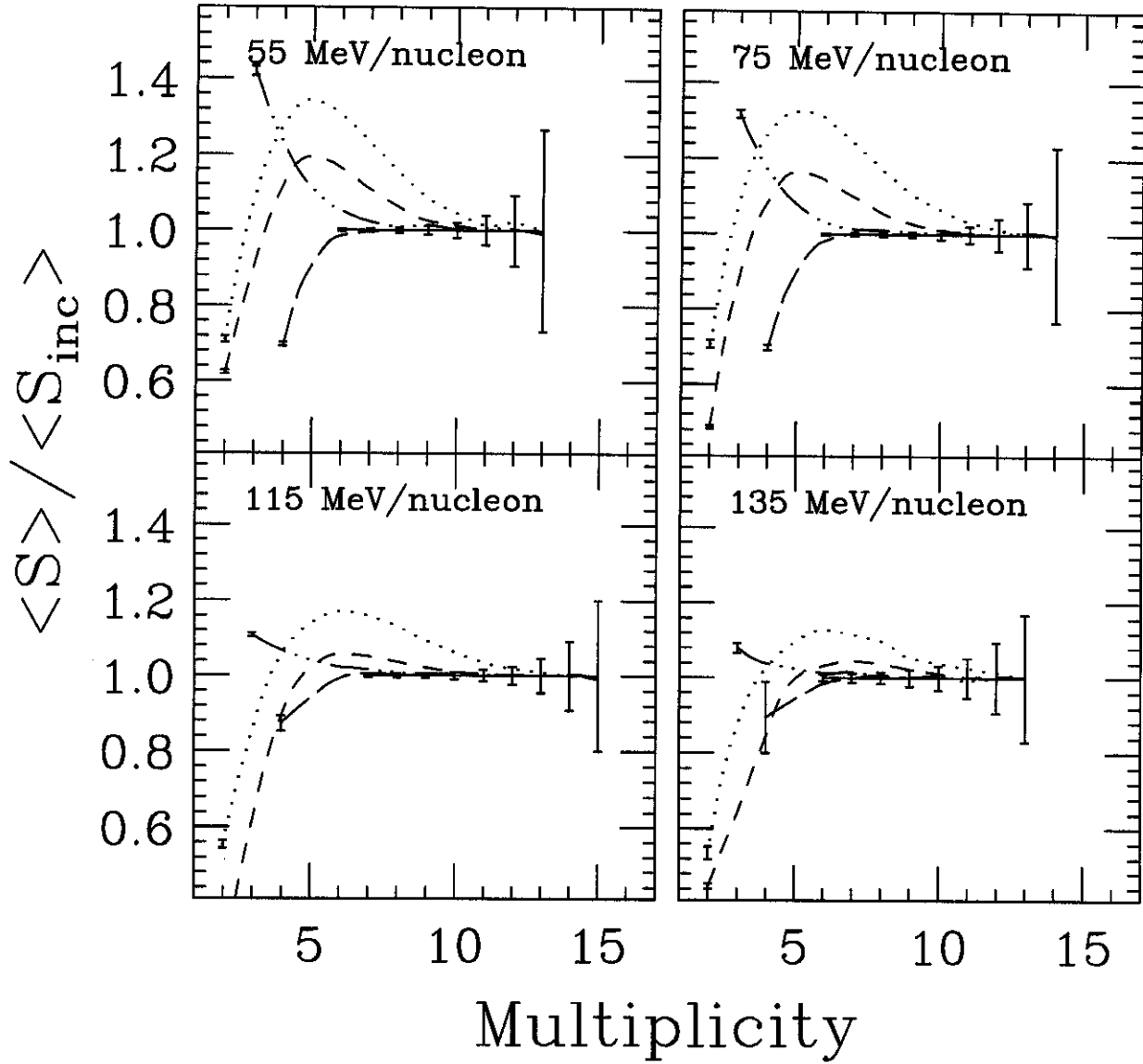
Figure 5: The same as Figure 4, but for the ^{20}Ne+^{27}Al reactions at 55, 75, 95, and 115 MeV/nucleon.
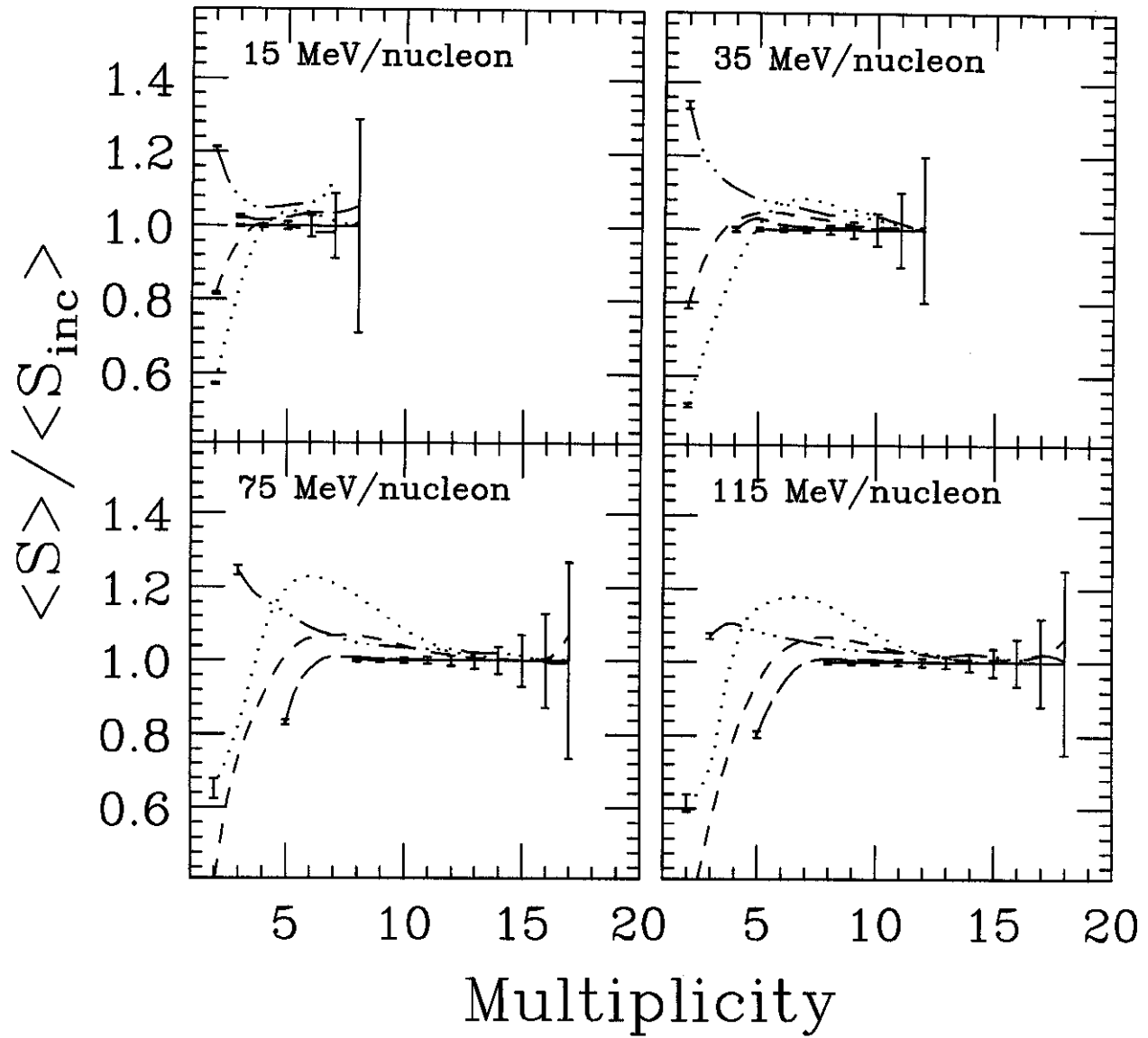
Figure 6: The same as Figure 4, but for the ^{40}Ar+^{45}Sc reactions at 15, 35, 75, and 115 MeV/nucleon.

Kr + Nb
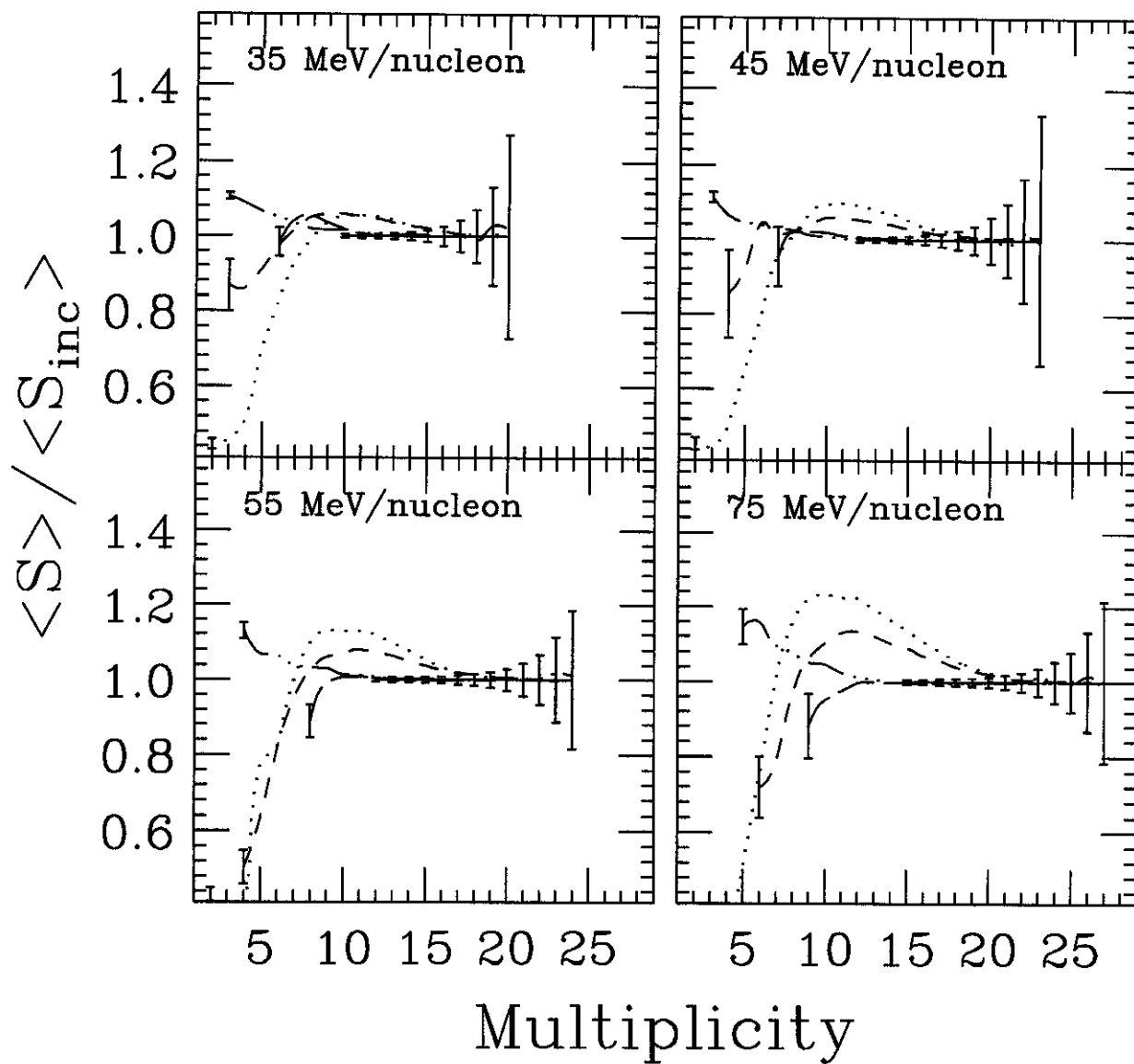
Figure 7: The same as Figure 4, but for the ^{84}Kr+^{93}Nb reactions at 35, 45, 55, and 75 MeV/nucleon.

Xe + La
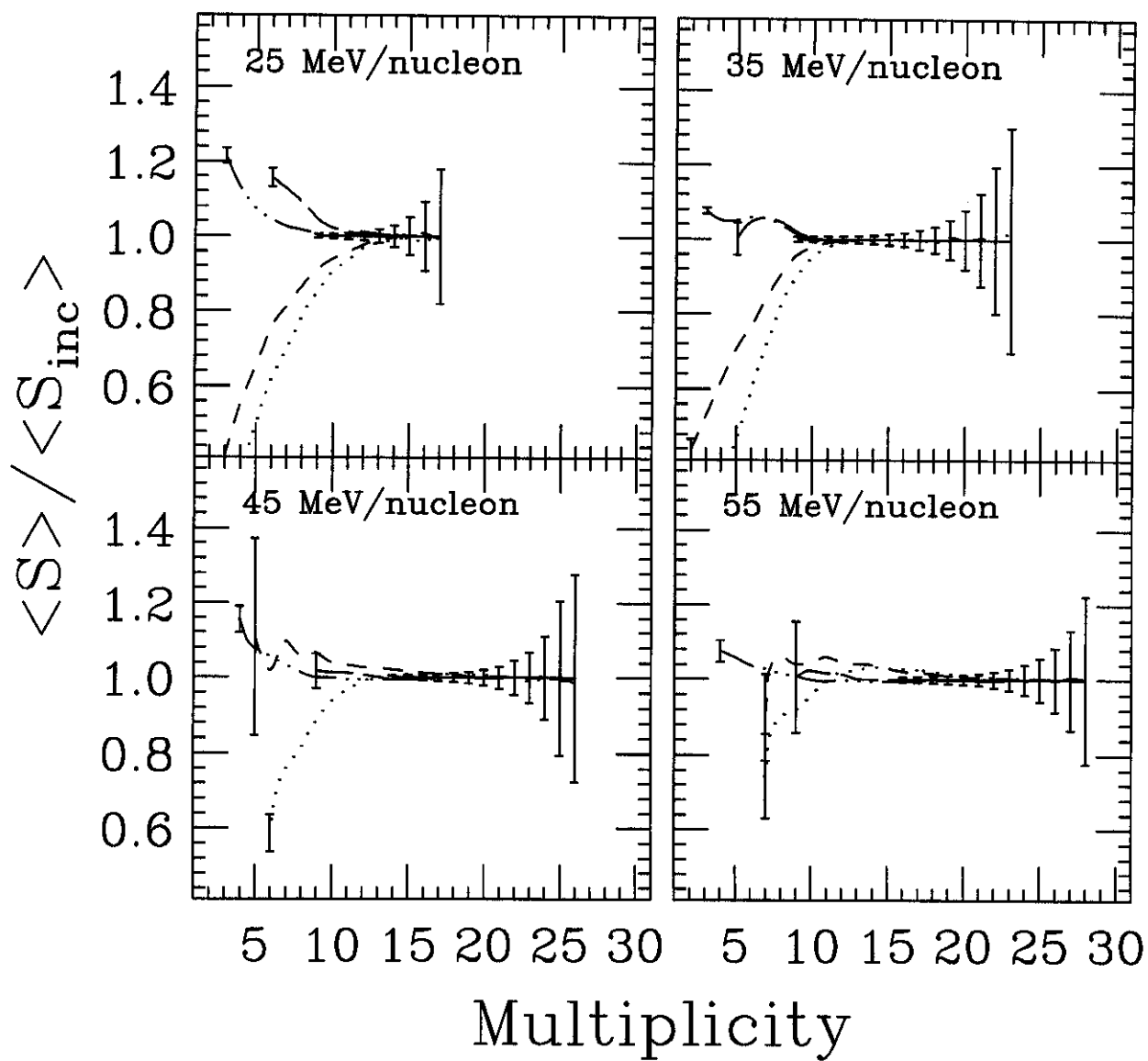
Figure 8: The same as Figure 4, but for the ^{129}Xe+^{139}La reactions at 25, 35, 45, and 55 MeV/nucleon.
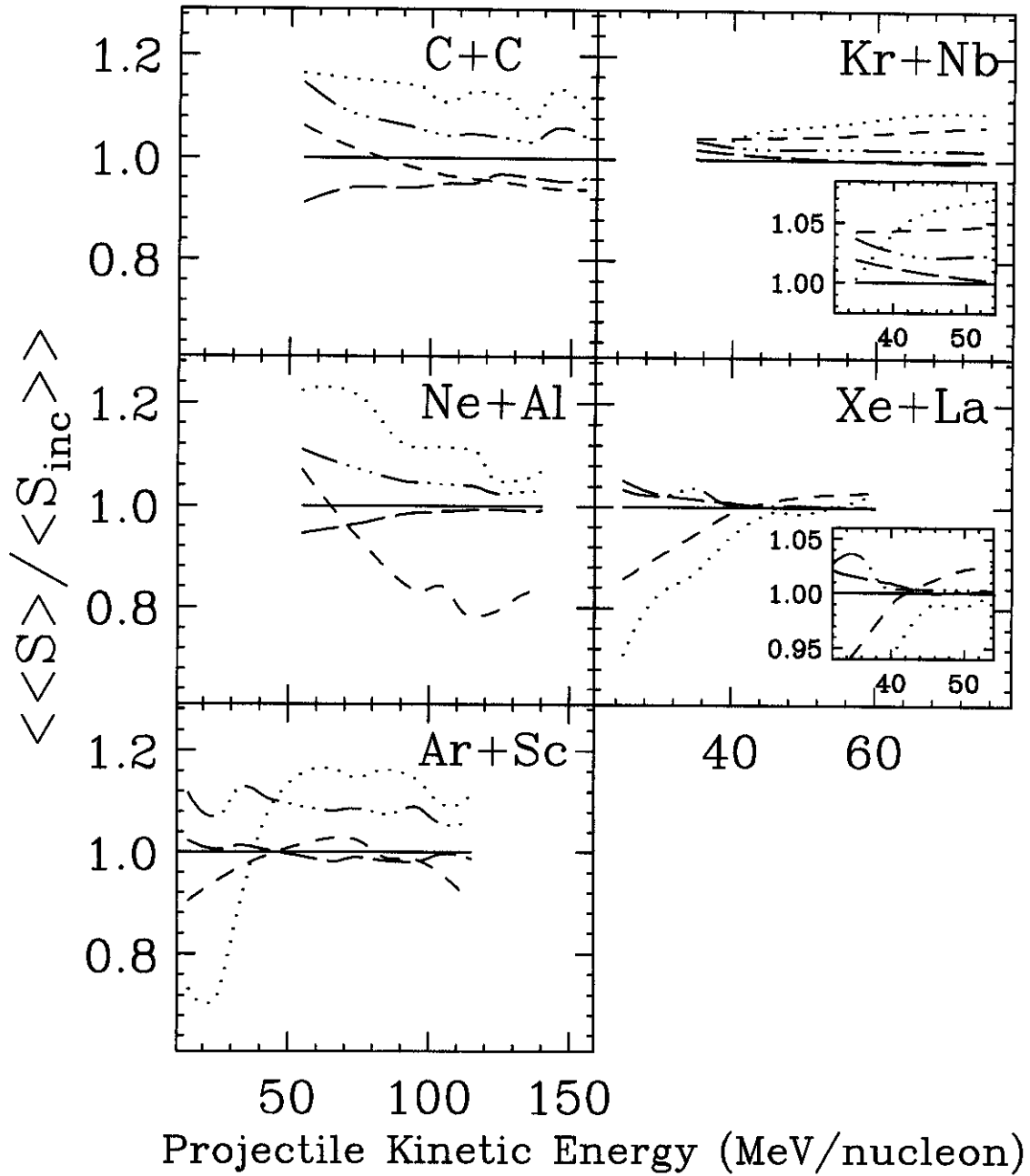
Figure 9: The weighted averages over the multiplicity of the curves shown in Figures 4 to 8 versus the projectile kinetic energy. Expanded views of the $^{84}Kr+^{93}Nb$ and $^{129}Xe+^{139}La$ results are inset for clarity.
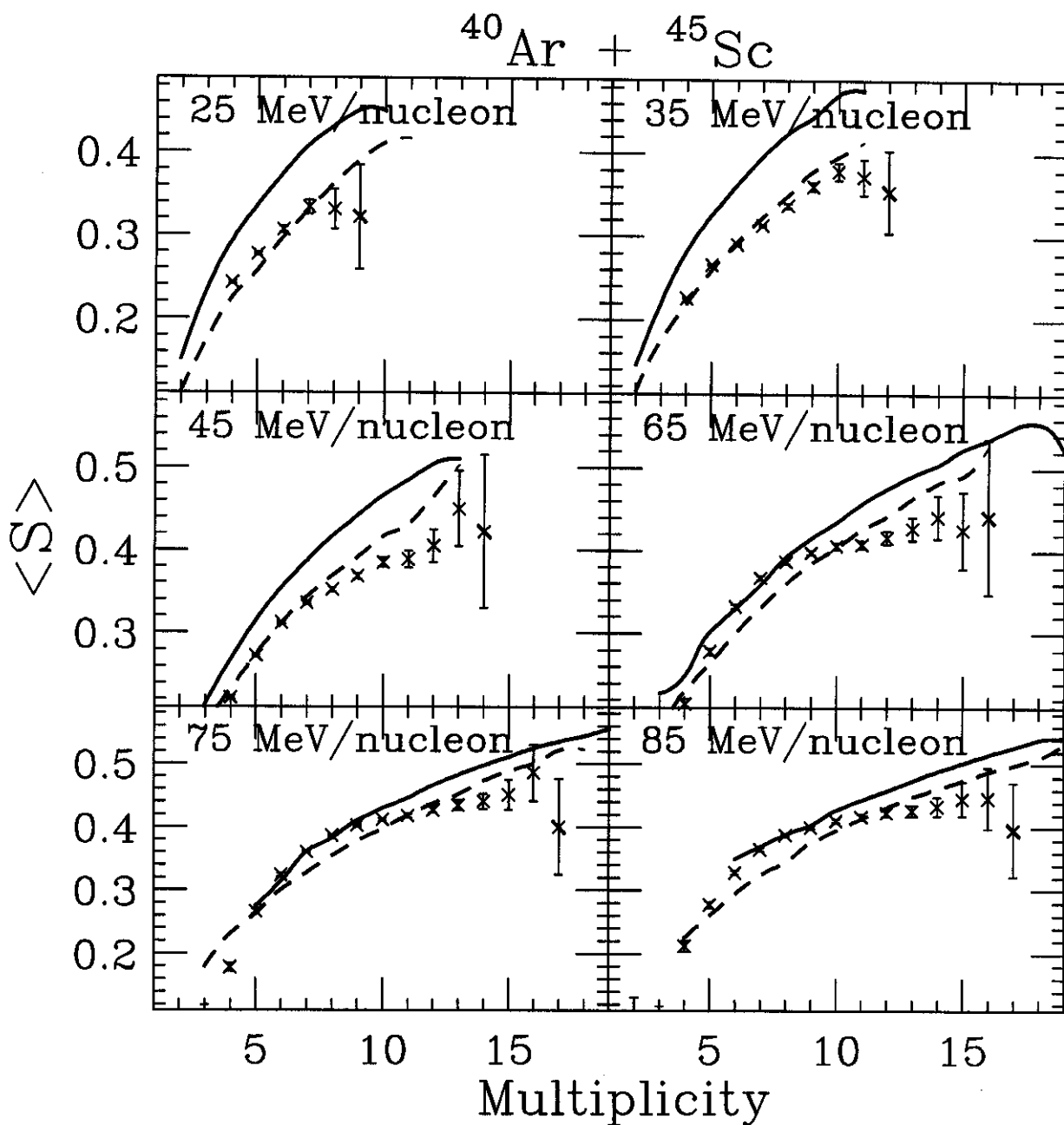
Figure 10: The average sphericity versus the total charged particle multiplicity for central ^{40}Ar+^{45}Sc reactions at beam energies of 25, 35, 45, 65, 75, and 85 MeV/nucleon. The experimental values are shown as the crossed points, while the solid(dashed) lines depict the predictions of the filtered MF(SB) models.
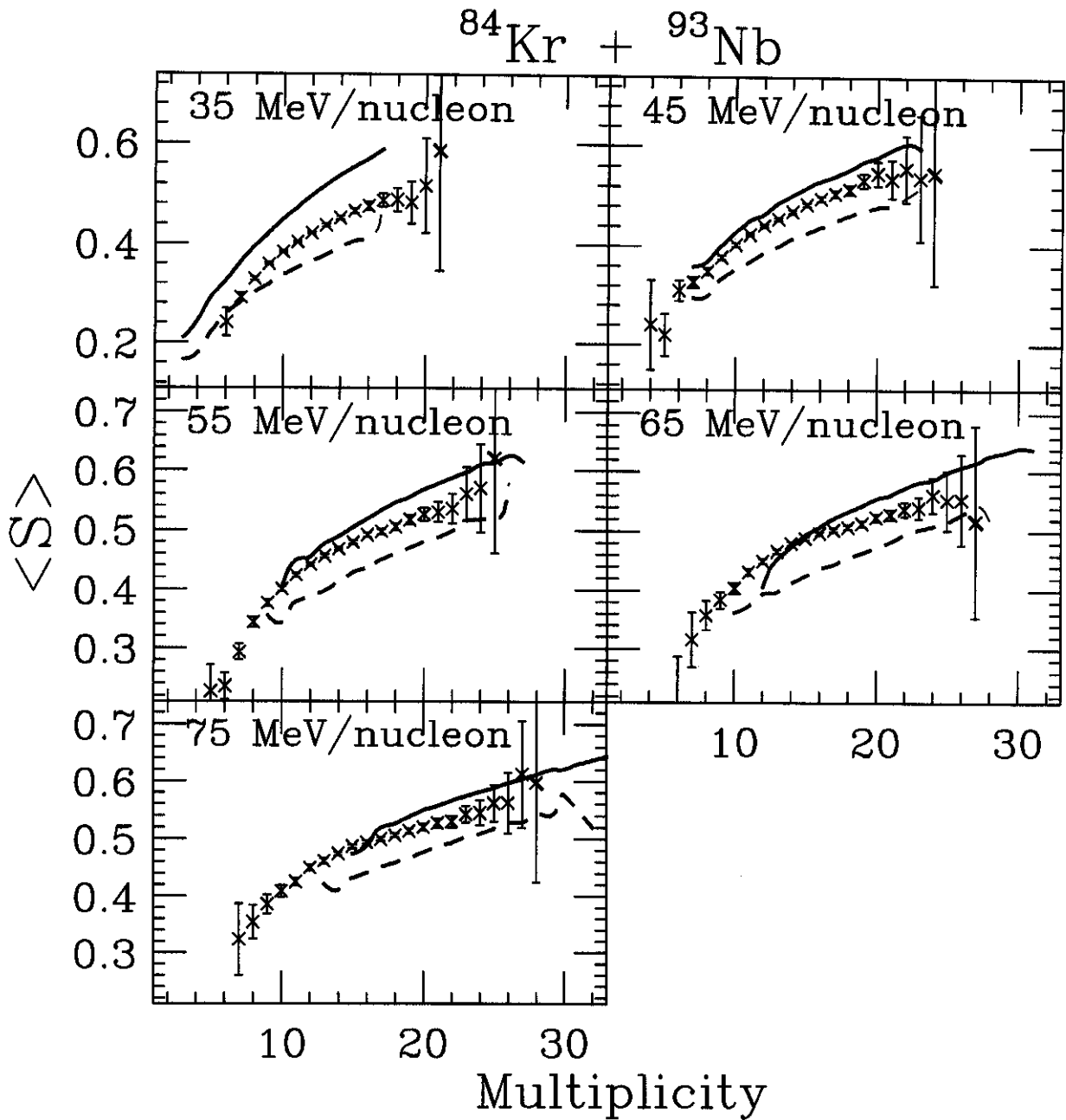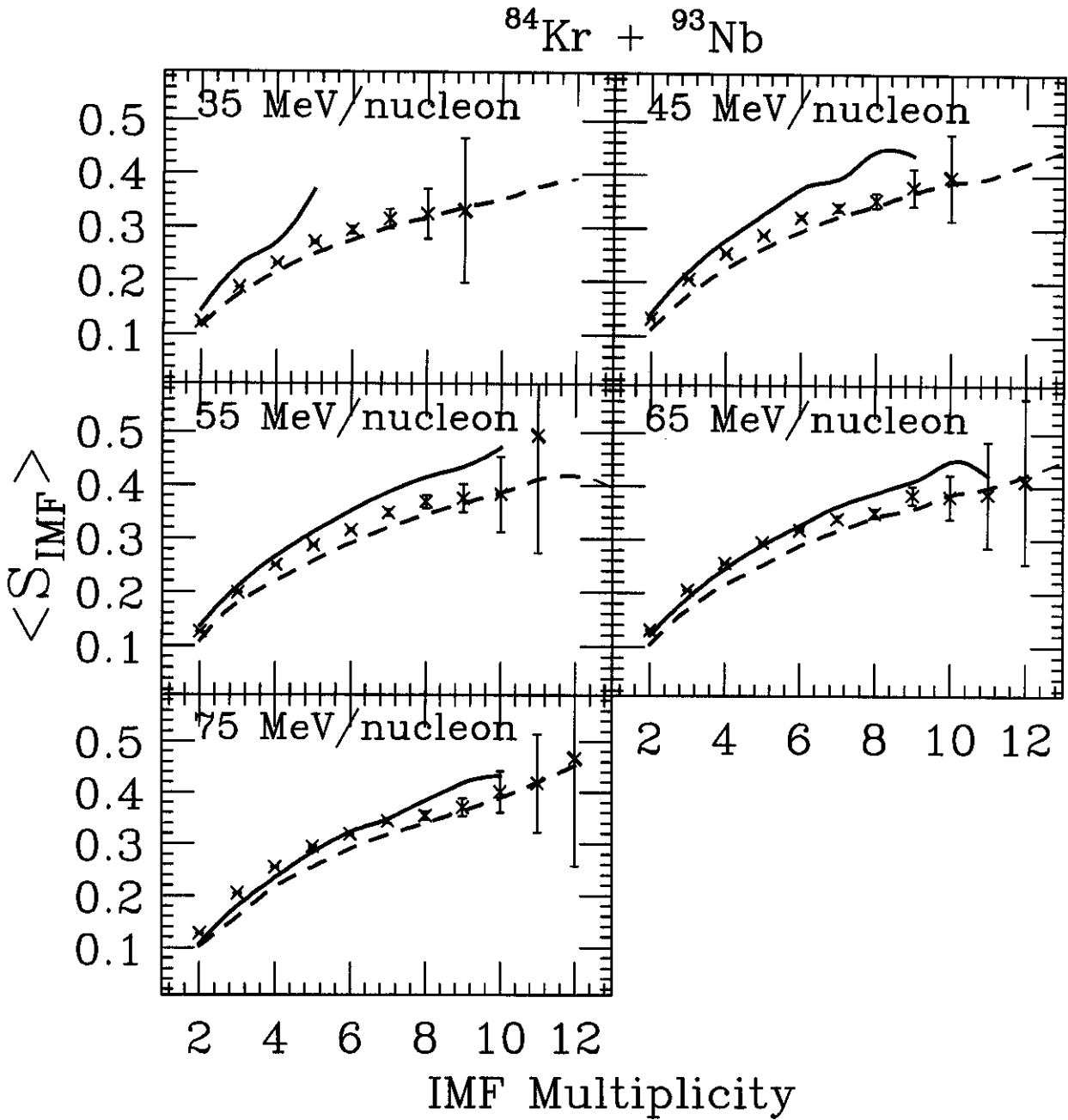
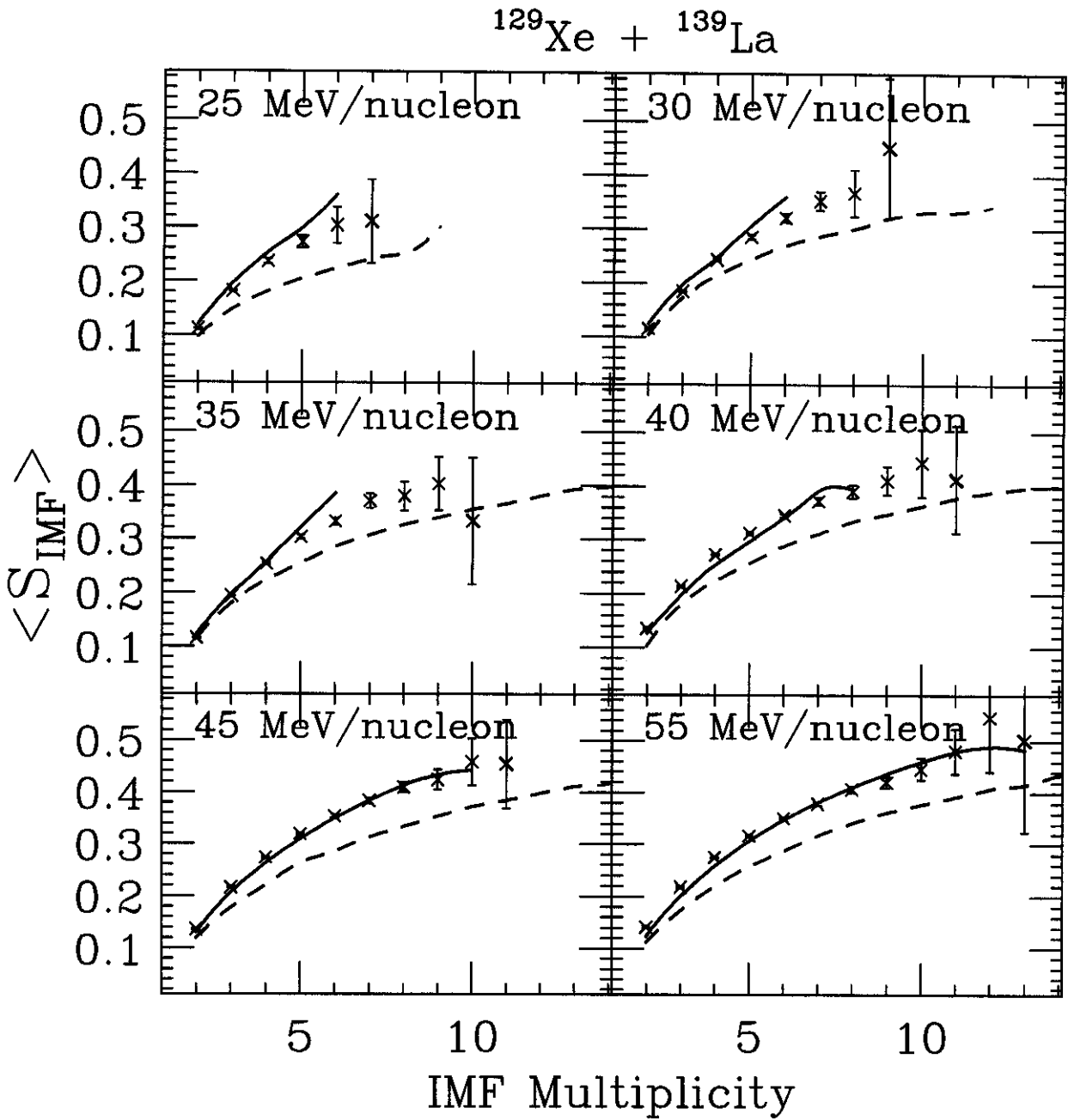Figure 11: The same as Figure 10, but for the ^{84}Kr+^{93}Nb reactions at 35, 45, 55, 65, and 75 MeV/nucleon.
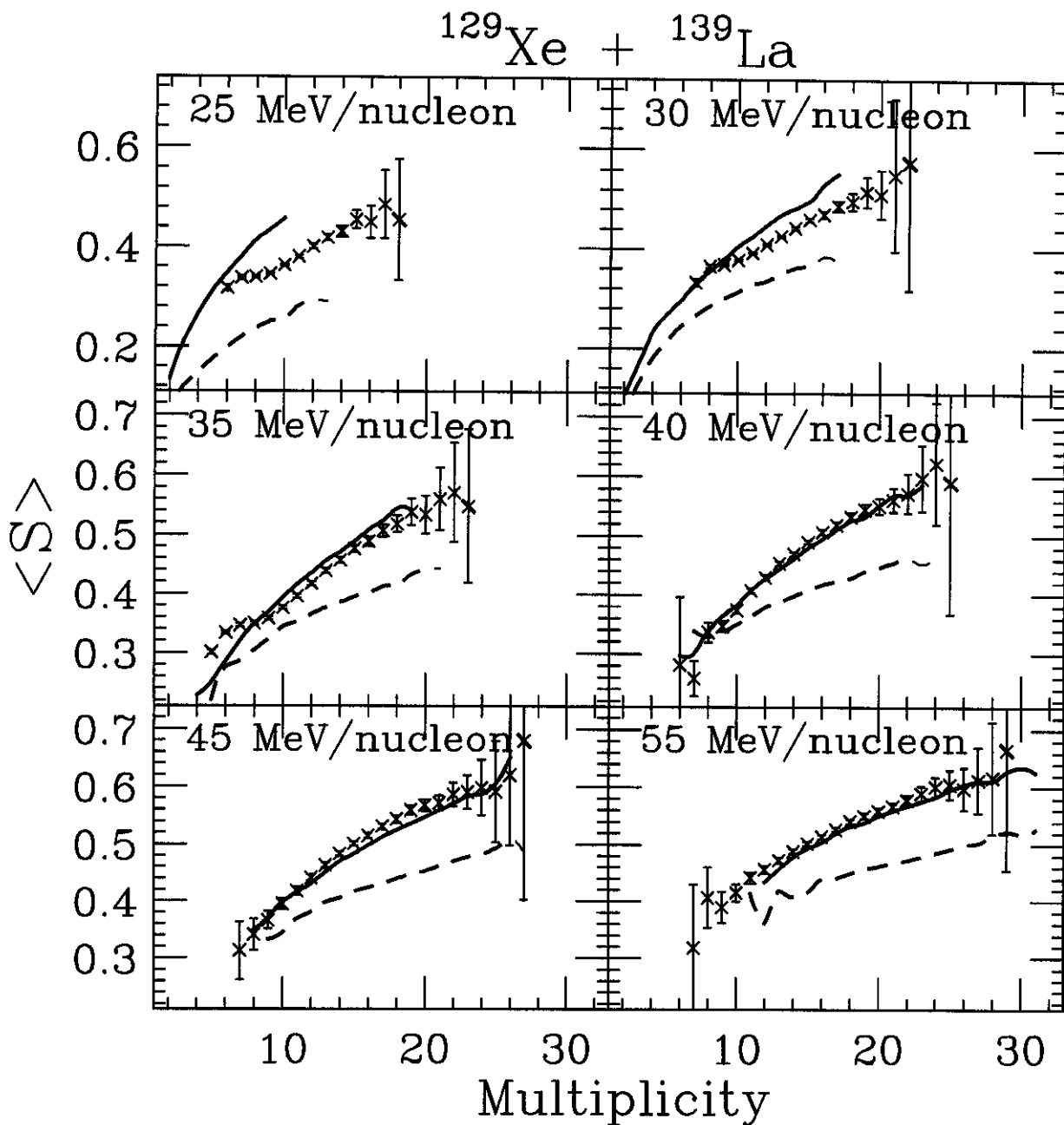
Figure 12: The same as Figure 10, but for the central ^{129}Xe+^{139}La reactions at 25, 30, 35, 40, 45, and 55 MeV/nucleon.
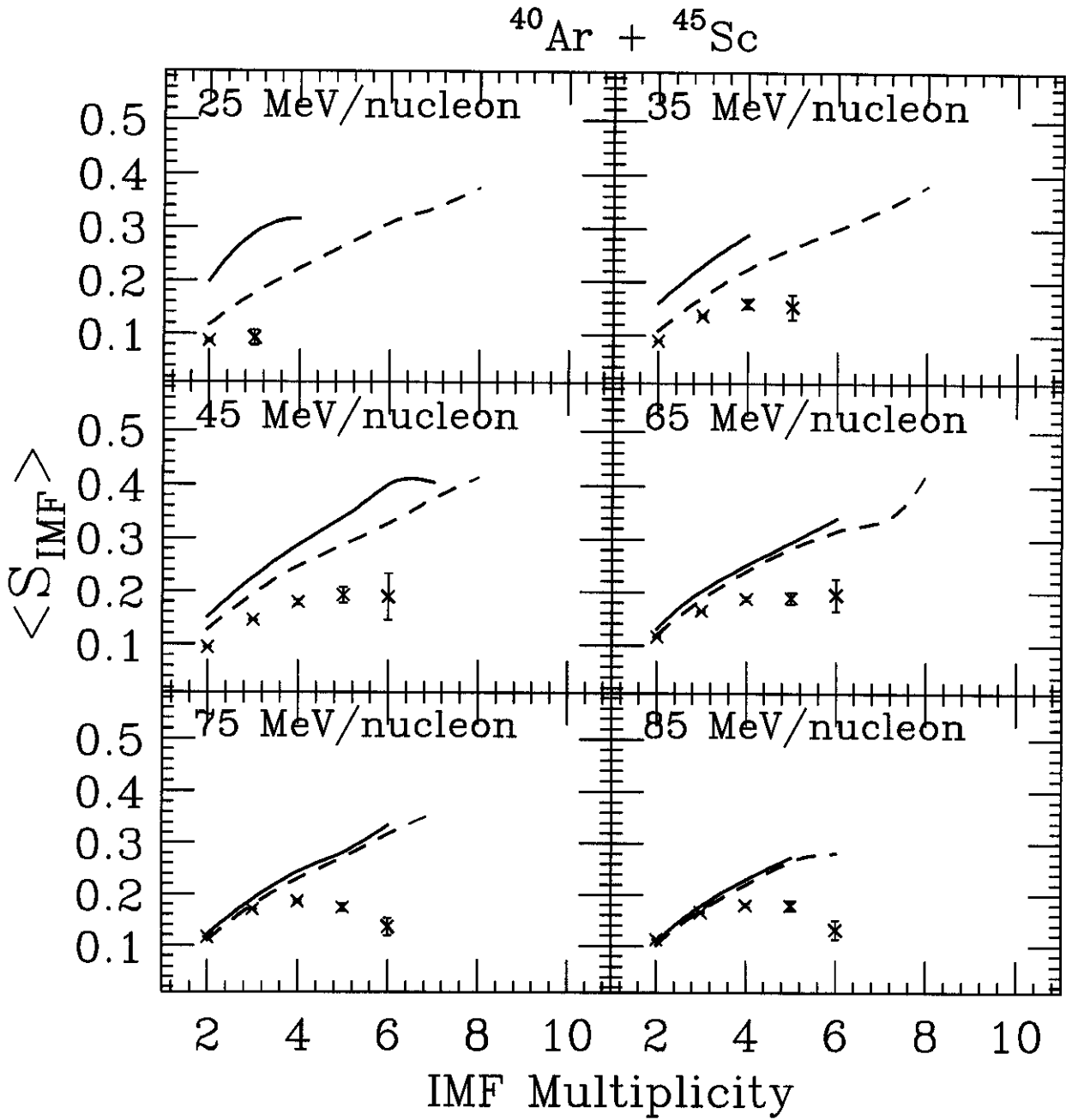
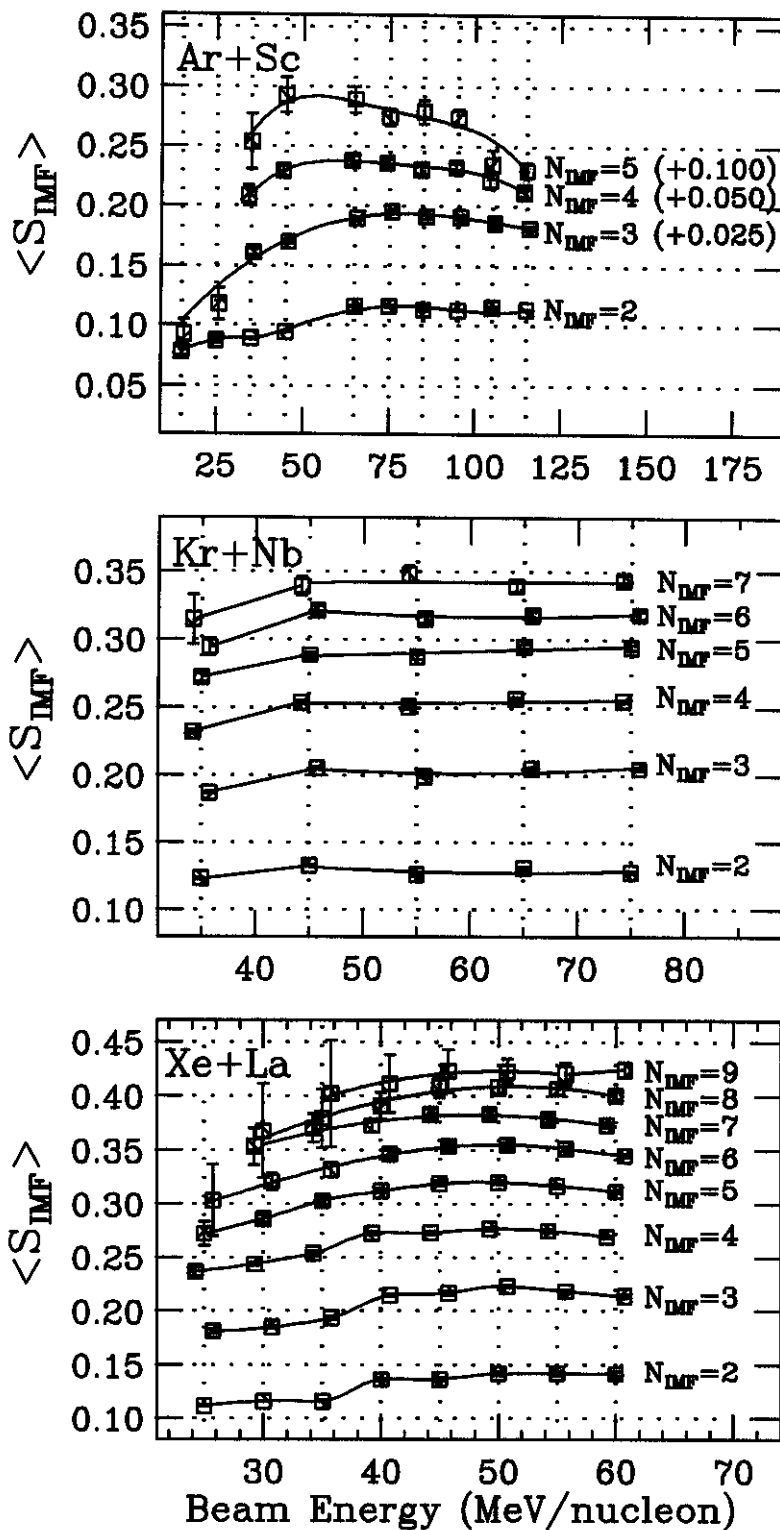Figure 13: The average IMF sphericity versus the total IMF multiplicity for central ^{40}Ar+^{45}Sc reactions at beam energies of 25, 35, 45, 65, 75, and 85 MeV/nucleon. The experimental values are shown as the crossed points, while the solid(dashed) lines depict the predictions of the filtered MF(SB) models.

$$^{84}\text{Kr} + {}^{93}\text{Nb}$$

Figure 14: The same as Figure 13, but for the $^{84}\text{Kr}+^{93}\text{Nb}$ reactions at 35, 45, 55, 65, and 75 MeV/nucleon.

Figure 15: The same as Figure 13, but for the central ^{129}Xe+^{139}La reactions at 25, 30, 35, 40, 45, and 55 MeV/nucleon.

Figure 16: The average IMF sphericity versus the beam energy for specific IMF multiplicities in the central ^{40}Ar+^{45}Sc, ^{84}Kr+^{93}Nb, and ^{129}Xe+^{139}La reactions.
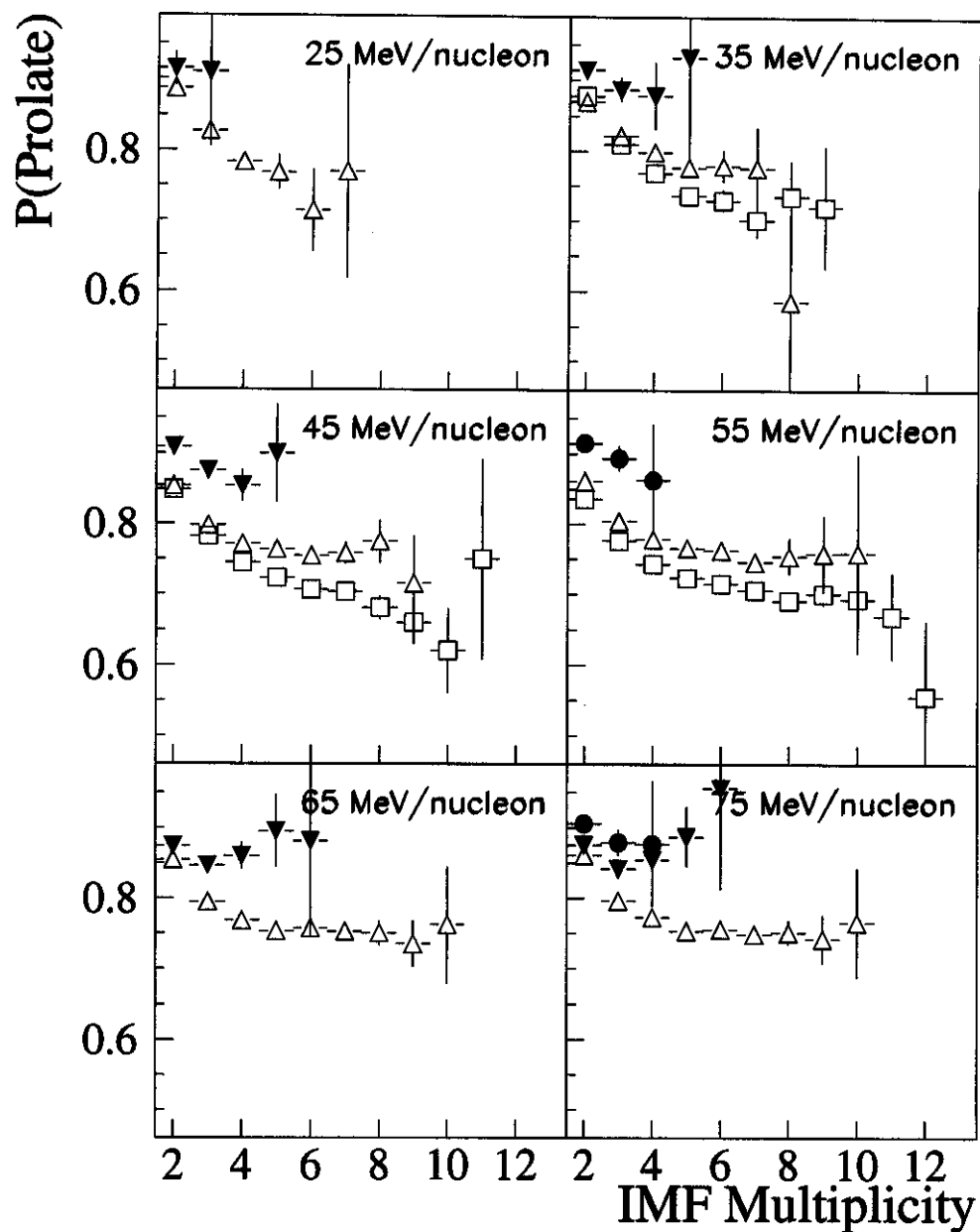
Figure 17: The probability for prolate IMF emission versus the IMF multiplicity for the central ^{20}Ne+^{27}Al (solid circles), ^{40}Ar+^{45}Sc (solid triangles), ^{84}Kr+^{93}Nb (open triangles), and ^{129}Xe+^{139}La reactions (open squares) at the beam energies listed in each frame. The specific definition of this probability is described in the text.
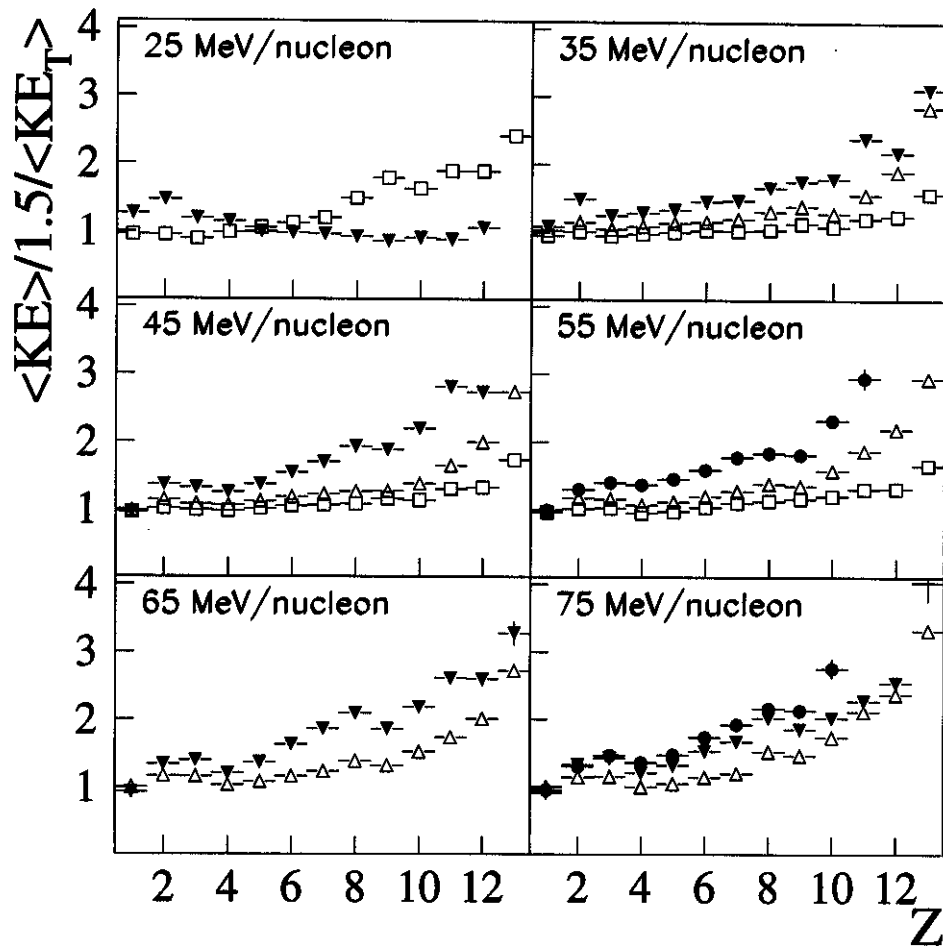
Figure 18: The ratio of the average kinetic energy and one and one half times the average transverse kinetic energy of the particles in the selected central events, versus the particle charge. The results for the ^{20}Ne+^{27}Al (solid circles), ^{40}Ar+^{45}Sc (solid triangles), ^{84}Kr+^{93}Nb (open triangles), and ^{129}Xe+^{139}La reactions (open squares) are shown.
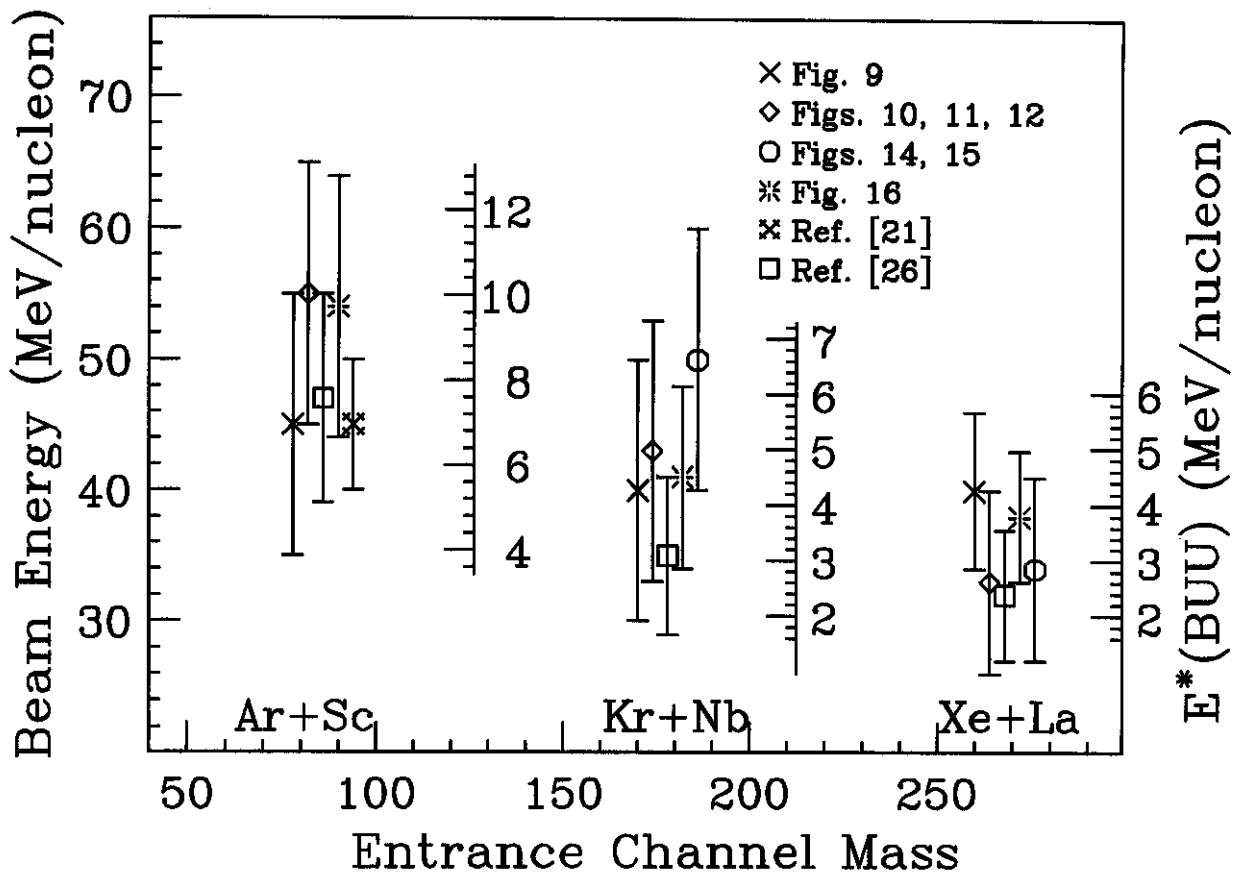
Figure 19: A summary of the results of the present shape analyses indicating transitions in various characteristics of the predominant reaction mechanisms for the systems formed in the central collisions in the different entrance channels. Predictions of the BUU calculations for the approximate excitation energies reached in the selected events are given for each entrance channel on the right side axes.